REPORT DOCUMENTATION PAGE

Form Approved OMB NO. 0704-0188

1. REPORT DATE (DD-MM-YYYY)	2. REPORT TYPE	3. DATES COVERED (From - To)
30-08-2013	MS Thesis	-

4. TITLE AND SUBTITLE
Bull's-Eye Structure with a Sub-Wavelength Circular Aperture

5a. CONTRACT NUMBER
W911NF-11-1-0024

5b. GRANT NUMBER

5c. PROGRAM ELEMENT NUMBER
611103

6. AUTHORS
Masoud Zarepoor

5d. PROJECT NUMBER

5e. TASK NUMBER

5f. WORK UNIT NUMBER

7. PERFORMING ORGANIZATION NAMES AND ADDRESSES
University of California - Irvine
5171 California Avenue, Suite 150

Irvine, CA 92697 -7600

8. PERFORMING ORGANIZATION REPORT NUMBER

9. SPONSORING/MONITORING AGENCY NAME(S) AND ADDRESS(ES)
U.S. Army Research Office
P.O. Box 12211
Research Triangle Park, NC 27709-2211

10. SPONSOR/MONITOR'S ACRONYM(S)
ARO

11. SPONSOR/MONITOR'S REPORT NUMBER(S)
58162-EL-MUR.47

12. DISTRIBUTION AVAILIBILITY STATEMENT
Approved for public release; distribution is unlimited.

13. SUPPLEMENTARY NOTES
The views, opinions and/or findings contained in this report are those of the author(s) and should not contrued as an official Department of the Army position, policy or decision, unless so designated by other documentation.

14. ABSTRACT
This research focuses on improving the spatial resolution of terahertz (THz) imaging. Using a sub-wavelength aperture in a metal ground plane is the most common way to improve the spatial resolution, but a sub-wavelength aperture has low radiation transmission. To increase the radiation transmission of a sub-wavelength aperture, periodic circular grooves were put in the metal around the aperture. The sub-wavelength circular aperture and the periodic circular grooves around it are known as the bull's-eye structure. The bull's-eye structure shows high

15. SUBJECT TERMS
Terahertz (THz) imaging, sub-wavelength aperture, bull's-eye structure, periodic circular grooves, spatial resolution, radiation transmission, High Frequency Structure Simulator (HFSS), CAD

16. SECURITY CLASSIFICATION OF:			17. LIMITATION OF ABSTRACT	15. NUMBER OF PAGES	19a. NAME OF RESPONSIBLE PERSON
a. REPORT	b. ABSTRACT	c. THIS PAGE			Peter Burke
UU	UU	UU	UU		19b. TELEPHONE NUMBER: 949-824-9326

Report Title

Bull’s-Eye Structure with a Sub-Wavelength Circular Aperture

ABSTRACT

This research focuses on improving the spatial resolution of terahertz (THz) imaging. Using a sub-wavelength aperture in a metal ground plane is the most common way to improve the spatial resolution, but a sub-wavelength aperture has low radiation transmission. To increase the radiation transmission of a sub-wavelength aperture, periodic circular grooves were put in the metal around the aperture. The sub-wavelength circular aperture and the periodic circular grooves around it are known as the bull’s-eye structure. The bull’s-eye structure shows high radiation transmission at its design frequency, and it also has sub-wavelength spatial resolution. This research designed the bull’s-eye structure to perform at ~3 mm wavelength in W band (75-110 GHz). Simulations were conducted on the 3D model of the bull’s-eye structure to study its performance in the desired frequency range. Then a bull’s-eye structure was fabricated and tested by the knife-edge technique to measure its spatial resolution. The knife-edge test results show the obtained sub-wavelength spatial resolution of the fabricated bull’s-eye structure. This research also includes the designs of a 500 GHz bull’s-eye structure and 100 GHz reflective probe.

Bull's-Eye Structure with a Sub-Wavelength Circular Aperture

A thesis submitted in partial fulfillment

Of the requirements for the degree of

Master of Science in Engineering

By

Masoud Zarepoor

B.S., Shiraz University, 2010

2013

Wright State University

WRIGHT STATE UNIVERSITY

GRADUATE SCHOOL

May 30, 2013

I HEREBY RECOMMEND THAT THE THESIS PREPARED UNDER MY SUPERVISION BY Masoud Zarepoor ENTITLED Bull's-Eye Structure with a Sub-Wavelength Circular Aperture BE ACCEPTED IN PARTIAL FULFILLMENT OF THE REQUIREMENTS FOR THE DEGREE OF Master of Science in Engineering.

_____

Joseph C. Slater, Ph.D., P.E
Thesis Director

_____

George Huang, Ph.D.

Chair, Department of Mechanical and Materials

Engineering College of Engineering and Computer Science

Committee on
Final Examination

_____

Joseph C. Slater, PhD., P.E

_____

Elliott R. Brown, PhD.

_____

Henry D. Young, PhD.

_____

R. William Ayres, Ph.D.
Interim Dean, Graduate School

ABSTRACT

Zarepoor Masoud. M.S. Department of Mechanical and Materials Engineering, Wright State University, 2013. Bull's-eye Structure with a Sub-Wavelength Circular Aperture.

This research focuses on improving the spatial resolution of terahertz (THz) imaging. Using a sub-wavelength aperture in a metal ground plane is the most common way to improve the spatial resolution, but a sub-wavelength aperture has low radiation transmission. To increase the radiation transmission of a sub-wavelength aperture, periodic circular grooves were put in the metal around the aperture. The sub-wavelength circular aperture and the periodic circular grooves around it are known as the bull's-eye structure. The bull's-eye structure shows high radiation transmission at its design frequency, and it also has sub-wavelength spatial resolution. This research designed the bull's-eye structure to perform at ~3 mm wavelength in W band (75-110 GHz).

Simulations were conducted on the 3D model of the bull's-eye structure to study its performance in the desired frequency range. Then a bull's-eye structure was fabricated and tested by the knife-edge technique to measure its spatial resolution. The knife-edge test results show the obtained sub-wavelength spatial resolution of the fabricated bull's-eye structure. This research also includes the designs of a 500 GHz bull's-eye structure and 100 GHz reflective probe.

ACKNOWLEDGEMENT

In the first place, I want to thank Dr. Elliott R. Brown for his great help and support during my research in the THz sensors group. Also, I thank Dr. Joseph C. Slater for his guidance and encouragement during my MS studies and my other committee member, Dr. Henry D. Young.

In addition, I appreciate John Middendorf, Dr. Matthieu Martin, Leamon Viveros, John Cetnar, and Mads Larsen for their helpful discussion and comments.

Finally, I thank Brandy Foster for her help with English grammar on my written Thesis document.

Table of Content

List of Figures

List of Tables

1. Introduction

1.1 Background

Much research has been conducted in the field of terahertz (THz) imaging due to the specific properties of THz waves. THz imaging has many applications in biomedical imaging, nondestructive monitoring, component testing, and quality inspection of products [2]. The spatial resolution of THz imaging is poor compared to infrared or visible imaging because the THz region corresponds to the wavelengths between tens of micrometer to one millimeter, so an improvement in the spatial resolution of the THz imaging needs to be accomplished. A common way to improve the spatial resolution is to use a sub-wavelength aperture [1].

Many researchers have studied the radiation transmission of an aperture. Bethe [3] and Bouwkamp [4] described the theoretical model of radiation going through the circular sub-wavelength aperture. They described the radiation going through an aperture in an infinitesimal opaque metallic screen. Also, they explained how the E-field of the transmitted radiation changes with distance from the aperture [5].

Any metal has a variable penetration depth in different spectral regions. Therefore, the thickness of a metal film should be much larger than its penetration depth in order to have negligible radiation transmission through the metal film compared to the radiation transmitted through a sub-wavelength aperture [5, 6].

In addition, many different shapes of apertures have been designed, such as a C-shaped [7], I-shaped [8], and H-shaped [9]. The main advantage of these alternative aperture shapes compared to a circular aperture is that they all have small gaps between their ridges. The E-field magnitude is large in the small gaps between the ridges, so this large E-field magnitude yields higher radiation transmission compared to a circular aperture. A sub-wavelength aperture reduces the signal strength. As a result, the main problem caused by a small aperture is the low radiation transmission. Therefore, the goal of this research is to enhance the radiation transmission of a small aperture.

Many designs have been proposed and tested in order to enhance the radiation transmission of a sub-wavelength aperture, and findings have shown that using a corrugated structure around an aperture should be an effective solution. When the incident radiation is focused to a spot size much larger than the aperture, it causes the resonant excitation of the surface waves (in the THz region) or the surface plasmons (in the optical region). The excitation of surface waves or surface plasmons is caused by the corrugated structure around the aperture. The corrugated structure around an aperture can have different shapes. The most common is the concentric, circular, periodic grooves surrounding a sub-wavelength aperture. This structure is known as a bull's-eye structure and can be fabricated on a metal plate or on a dielectric substrate covered with a thin metal film. Finally, the excited surface waves or surface plasmons concentrate at the center of the structure, which results in more radiation transmission [1, 5].

In the visible region, Thio et al. (2001) studied the optical radiation transmission through a sub-wavelength aperture in a metal film surrounded by concentric, periodic grooves. They observed three times more radiation transmission for this design than the

circular aperture without the corrugated surface. Thio et al. (2002) then used the bull's-eye structure for near-field scanning applications [10, 11].

Lezec et al. (2002) studied the radiation through a sub-wavelength aperture and noted that it diffracts with a large angular divergence. By fabricating periodic grooves around the aperture, they observed that the radiation had a much smaller angular divergence, and could be controlled in the direction of the radiation [12].

Akarca-Biyikli, Bulu, and Ozbay, (2004) investigated theoretically and experimentally the microwave radiation transmission through a sub-wavelength aperture in a corrugated metal plate, and measured the transmission of the fabricated structures in the 8-30 mm wavelength range. They obtained ~50 % radiation transmission with small angular divergence radiation for their designed structures [13].

Mahboub et al. (2010) theoretically and experimentally investigated the optimal geometric parameters of a bull's-eye structure in the optical region. They found that the geometric parameters in the bull's-eye structure are interlinked. To illustrate, they found the relationship between the design resonant wavelength and periodicity of the grooves, as well as the relationship between the other geometric parameters with the design resonant wavelength. Their results indicate the ability to fabricate a bull's-eye structure with the optimal radiation transmission at the desired frequency [14].

In the THz region, Ishihara et al. (2005) studied the radiation transmission through a bull's-eye structure with a sub-wavelength circular aperture. The bull's-eye structure was fabricated in a metal plate. Their designed bull's-eye structure had 20 times more THz radiation transmission than a circular aperture without periodic structure at the

design frequency of 1.5 THz. Also, they reached a sub-wavelength resolution (λ/4) at the design frequency [5, 15].

Then Ishihara et al. (2006) designed a bull's-eye structure with a bow-tie aperture. Instead of using a thick metal plate for their design, they used a corrugated dielectric substrate covered with a thin metal film. They reached a spatial resolution of 12 μm (λ/17) in the near-field region [1, 5].

Finally, a bull's-eye structure can be used for sub-wavelength resolution transmission imaging around 100 GHz. A small feature (such as skin-cancer tissue) should be placed in the near-field region of a bull's-eye aperture on its transmission side for imaging purposes. Bull's-eye structures are used for imaging small features because normal optical components in this frequency region are limited to diffraction-limited resolution, which is typically several wavelengths. Additionally, these optical components are not appropriate for detecting features with a sub-wavelength size and obtained images, having these optical components as transmission devices, do not have high contrast.

1.2 Overview

The object of this research is to design and fabricate a bull's-eye structure with a sub-wavelength circular aperture to perform at a wavelength of ~3 mm in W band (75-110 GHz). This bull's-eye structure can be used for skin tissue detection, such as detecting skin burns and melanoma. The designs of a 500 GHz bull's-eye structure (with an application in biological sensing and detection) and a 100 GHz silicon reflective probe (with an application in identifying melanoma and skin burns) are also carried out. It is necessary to note that this research is not limited to design and computer simulation of

bull's-eye structures, and it has significant fabrication and experimentation. Bull's-eye structures were fabricated with high precision using a CNC lathe machine and a thermal evaporator. Then, quality of fabricated bull's-eye structures was evaluated by conducting thorough experimental measurements with a pretty complex setup.

This Thesis contains six chapters. In the second chapter, the designs of 3-mm-wavelength and 500 GHz bull's-eye structures are presented. In the third chapter, the simulation results for the designed bull's-eye structures are presented. The simulation results show the computed transmission spectra for the designed bull's-eye structures in the desired frequency ranges. The fabrication process of the 3-mm-wavelength bull's-eye structure is also demonstrated in the third chapter. In the fourth chapter, the experimental results for the fabricated 3-mm-wavelength bull's-eye structure are presented. The experimental results show the measured spatial resolution of the fabricated bull's-eye structure. The simulation results for the designed 100 GHz reflective probe are reported in the fifth chapter. The conclusion of the Thesis is presented in the sixth chapter.

2. Design of the Bull's-Eye Structure with a Sub-Wavelength Circular Aperture

2.1 Design and Dimensions of the Bull's-Eye Structure

The bull's-eye structure consists of a corrugated dielectric substrate covered with a thin metal film with five geometric parameters. These parameters are aperture diameter (d), periodicity of the grooves (p), width of the grooves (w), depth of the grooves (s), and thickness of the metal film (t). The bull's-eye structure is fabricated on a dielectric substrate instead of a metal plate because a thick metal plate reduces the radiation transmission. The main goal is to design a bull's-eye structure with a sub-wavelength circular aperture that has a resonant wavelength of approximately 3 mm, in the common W band (75-110 GHz) [1, 5].

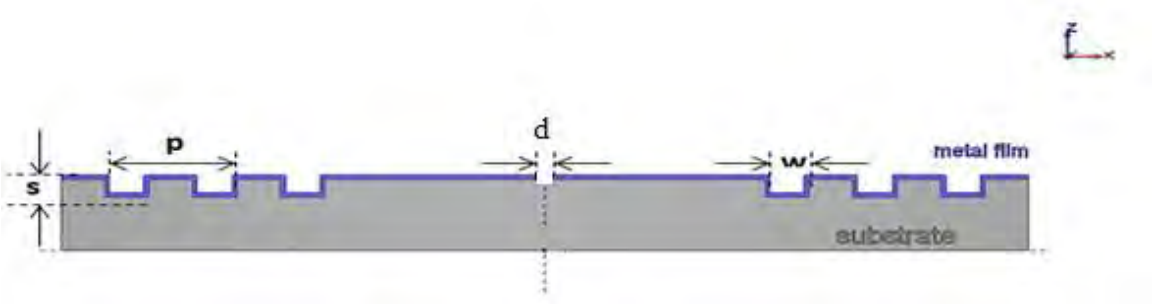

Figure 1. The cross section of a bull's-eye structure showing an aperture in a metal film with 3 periodic grooves around the aperture.

Previously, Ishihara et al. (2006) designed a bull's-eye structure with a bow-tie aperture that had a radiation peak at a wavelength of 207 μm (1.45 THz). There were two peaks for the bull's-eye structure; one was a peak in the transmission spectrum due to the bow-tie aperture, and the other peak was due to the resonant excitation of the surface waves of the bull's-eye structure (BE). To have the highest possible radiation transmission, both peaks should coincide [1].

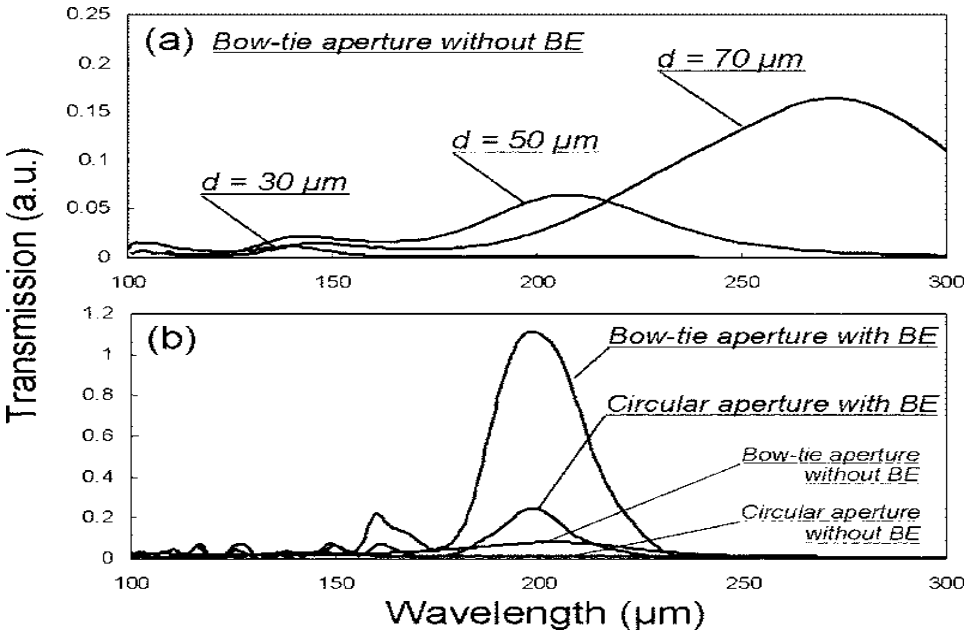

Figure 2. Computed radiation transmission for the (a) bow-tie aperture (b) bow-tie aperture and circular aperture with and without bull's-eye structure (BE) [1].

Figure 2 therefore demonstrates the rationale for designing the bull's-eye structure. In Figure 2 (a), there are different transmission spectra for the bow-tie apertures with the different diameters. Each has a radiation peak at a specific wavelength. The

bow-tie aperture having the diameter of 50 μm has the peak at the desired wavelength of 207 μm, so this bow-tie aperture was used in the Ishihara et al. (2006) design [1].

In Figure 2 (b), the designed bull's-eye structure has a peak at the desired design wavelength (207 μm). For the bull's-eye structures, the one with a bow-tie aperture and the one with a circular aperture, high radiation transmission improvements exist compared to the bow-tie and circular apertures without the bull's-eye structure.

It should be noted that the bull's-eye structure with the bow-tie aperture has higher radiation transmission compared to the bull's-eye structure without the bow-tie aperture because of the sharp tips of the bow-tie aperture. Table 1 summarizes the parameters of the bull's-eye structure with a sub-wavelength circular aperture that Ishihara et al. (2006) designed for the resonant wavelength of 207 μm [1].

Table 1. Bull's-eye structure parameters designed by Ishihara et al. (2006) [1].

Resonant Wavelength	207 μm
Width of grooves (w)	66 μm
Periodicity of grooves (p)	132 μm
Depth of grooves (s)	13 μm
Thickness of gold film	0.4 μm
Diameter of aperture	50 μm
Refractive index of substrate	Resin, 1.5
Angle of incident wave	Normal, from the substrate side

The research goal is to use the bull's-eye structure with a sub-wavelength circular aperture at a much longer wavelength of ~3 mm (3000 μm). Therefore, the dimensions for this bull's-eye structure can be found by a 15-times scaling of the Ishihara et al. (2006) design, as summarized in Table 2 [1].

Table 2. Bull's-eye structure parameters (designed to perform at ~3 mm wavelength).

Resonant Wavelength	~3 mm (3000 micron)
Width of grooves (w)	0.99 mm
Periodicity of grooves (p)	1.98 mm
Depth of grooves (s)	0.195 mm
Thickness of silver film	1 μm
Diameter of aperture	750 μm
Refractive index of substrate	Teflon, n = 1.45 ($\varepsilon_r = 2.1$)
Angle of incident wave	Normal, from the substrate side

In Table 2, ε_r is the relative permittivity. Teflon was used for the bull's-eye structure substrate because it is transparent in the THz region. Additionally, a silver film was used instead of a gold film. Silver is a highly conductive metal and would be a good replacement for the gold film because it is much cheaper.

Also, the goal is to design a bull's-eye structure with a sub-wavelength circular aperture that has resonant frequency of at least 500 GHz. The dimensions of this bull's-eye structure are approximately one-fifth of the dimensions of the bull's-eye structure designed for ~3 mm wavelength.

Table 3. Bull's-eye structure parameters (designed to perform at 500 GHz).

Resonant Frequency	500 GHz
Width of grooves	191 μm
Periodicity of grooves	382 μm
Depth of grooves	37 μm
Thickness of silver film	1 μm
Diameter of aperture	144 μm
Refractive index of substrate	Teflon, n = 1.45 ($\varepsilon_r = 2.1$)
Angle of incident wave	Normal, from the substrate side

Table 3 shows the designed 500 GHz bull's-eye structure with a sub-wavelength circular aperture parameters. In addition, it should be emphasized that the goal of this research is to design the bull's-eye structure with a sub-wavelength circular aperture and not a bow-tie aperture, but the Ishihara et al. (2006) design procedure for the bull's-eye structure with a bow-tie aperture was explained because the similar design procedure was used in this research [1]. In order to check the accuracy of this design and to evaluate the performance of the designed bull's-eye structures with the above dimensions in the desired frequency ranges, simulations were carried out on the designed bull's-eye structures using electromagnetic software called High Frequency Structure Simulator (HFSS).

3. Simulation and Fabrication of the Bull's-Eye Structure with a Sub-Wavelength Circular Aperture

3.1 Introduction to HFSS

HFSS uses the finite element method (FEM) to solve Maxwell's equations for the electromagnetic fields when no analytic solution exists for them. This is particularly true for complex geometries and boundary conditions. The elements used by HFSS are three dimensional tetrahedra. HFSS uses a conformal, adaptive system of meshing, meaning that it creates a large number of elements in the regions where the field shows large variation, but it uses a smaller number of elements in the regions with lower field variation. Then HFSS compares the results of the current mesh to the previous mesh until the solution is converged to the user defined error [16, 17, 18].

3.2 HFSS Settings

3.2.1 Boundary Condition and Excitation

The bull's-eye structure is first created geometrically within an air-filled box, as shown in Figure 3. Radiation boundary conditions are assigned to the four sides of the box. For the radiation boundary condition, no reflection occurs, and the entire radiation incident on the boundary is absorbed.

A wave port excitation is assigned to the top and bottom faces of the air box. Wave port excitation enables a frequency-sweep analysis of the problem, so it enables the radiation transmission study of a bull's-eye structure over a desired frequency range.

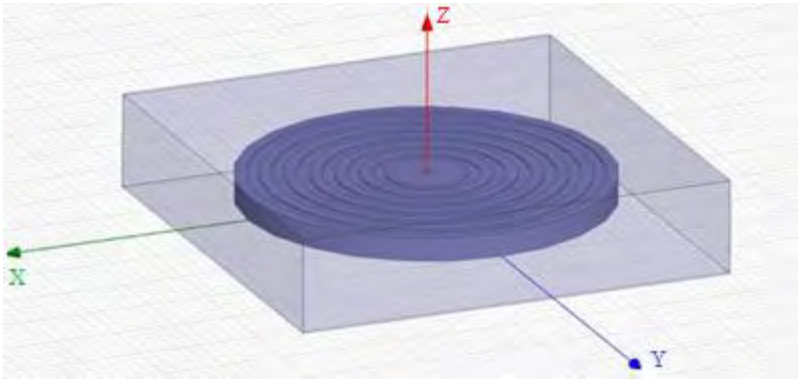

Figure 3. Designed bull's-eye structure with a circular aperture in HFSS.

Figure 3 shows the designed bull's-eye structure substrate in the air-filled box. The six concentric, periodic grooves around the circular aperture can be observed. The radiation is propagating along the Z-axis (normal to the substrate), and the polarization of the radiation is along the Y-axis.

3.3 Simulation Results for the 3-mm-Wavelength Bull's-Eye Structure

3.3.1 Aperture Diameter Optimization for the 3-mm-Wavelenght Bull's-Eye Structure

The parameters of the 3-mm-wavelength bull's-eye structure with a varying aperture diameter are summarized in Table 4. The aperture diameter varies from 0.2 mm to 2.2 mm with 0.2 mm step size.

Table 4. 3-mm-wavelength bull's-eye structure parameters (aperture diameter optimization).

Frequency Sweep	90 -100 GHz
Width of grooves (w)	0.99 mm
Periodicity of grooves (p)	1.99 mm
Depth of grooves (s)	0.195 mm
Thickness of silver film (t)	1 μm
Diameter of aperture (d)	0.2-2.2 mm
Refractive index of substrate	Teflon, n = 1.45 ($\varepsilon_r = 2.1$)
Angle of incident wave	Normal, from the substrate side

HFSS allows for the optimization of transmission or other electromagnetic characteristics by varying geometrical or material parameters. In this case, all the geometric parameters of the bull's-eye structure were held constant except the aperture diameter, which was varied parametrically to maximize the radiation transmission. The end goal is an aperture diameter which has both high radiation transmission and also small spatial resolution. Studying the bull's-eye structure with different aperture diameters allows for the selection of an aperture diameter which has these desired features. Also, it should be emphasized that other bull's-eye parameters, which are depth of grooves(s), width of grooves (w), periodicity of grooves (p), were held constant because periodic grooves parameters (s, w, p) are correlated and constrained by Ishihara et al. (2006) design.

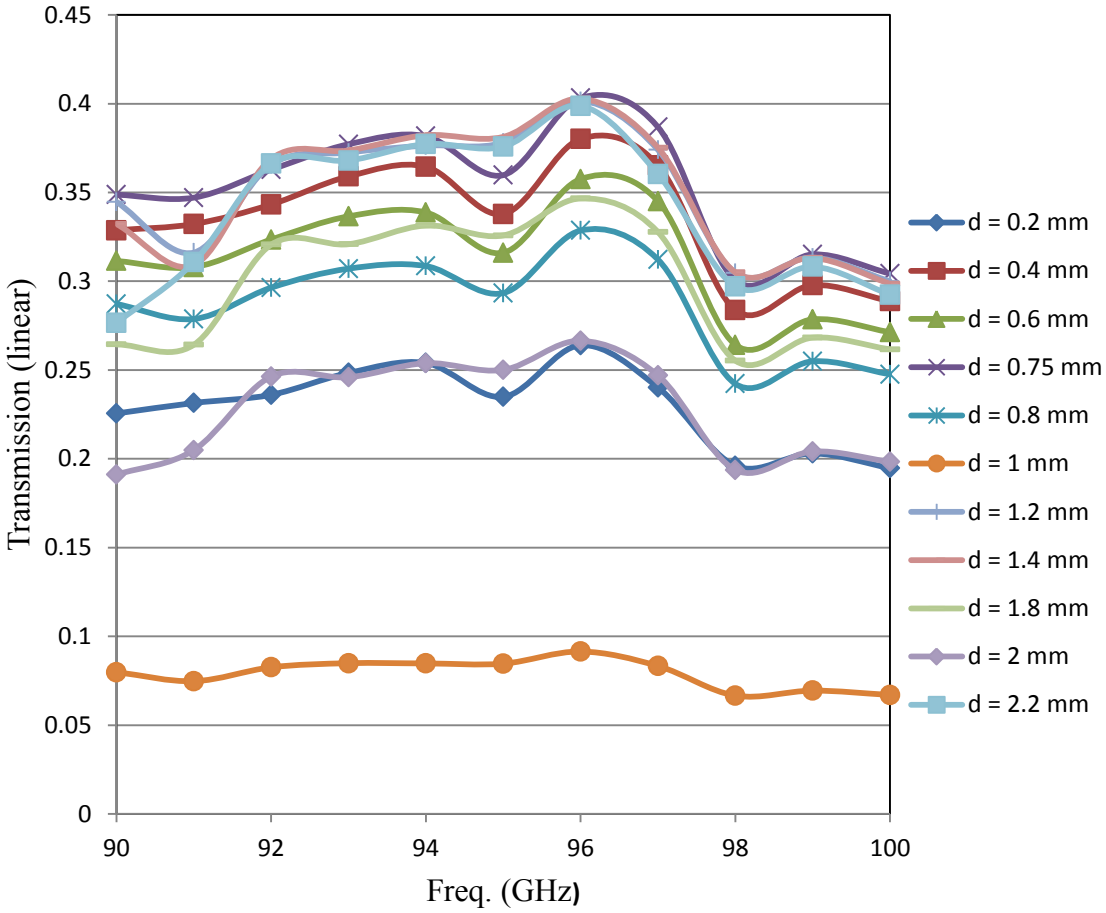

Figure 4. Computed radiation transmission for the bull's-eye structure with different aperture diameters (d).

As shown in Figure 4, the bull's-eye structure with an aperture diameter of 0.75 mm has the highest radiation transmission in the 90-100 GHz frequency range. The bull's-eye structures with the aperture diameters of 2.2 mm and 1.4 mm have radiation transmission close to the bull's-eye structure having an aperture diameter of 0.75 mm, but the 0.75 mm aperture diameter was selected because it has smaller spatial resolution. Knife-edge tests were used for measuring the spatial resolution of the bull's-eye structure in this research. The knife-edge resolution test is defined by a sharp knife edge that is

laterally displaced so that it blocks from 90% to 10% of the transmitted signal strength through the aperture (the spatial resolution measurement for the bull's-eye structure with an aperture diameter of 0.75 is explained in the fourth chapter) [5].

There are many publications regarding the bull's-eye structure design in different spectral regions. They measured the bull's-eye structures radiation transmission in the near-field region because the enhanced radiation transmission seen in a bull's-eye structure is mainly an effect of evanescent waves, caused by the corrugated metal surface, transmitting through the aperture. The near-field region of a bull's-eye structure is located on the transmission side and within one aperture diameter of the structure. The evanescent waves are of high magnitude in the near-field region, so the goal of this research is to study the near-field radiation transmission of the bull's-eye structure [5].

As the simulations of the bull's-eye structure evolved, it became evident that the transmission spectrum was dependent on the distance of the wave ports from the bull's-eye structure (this dependence is explained in sections 3.3.2-3.3.4). So the radiation transmission was computed at three typical distances: (1) 1 mm from the bull's-eye structure (~one-third of the excitation wavelength), (2) 0.5 mm from the bull's-eye structure, which is located in the near-field region, and (3) 3 mm (= excitation wavelength) away from the bull's-eye structure.

3.3.2 3-mm-Wavelength Bull's-Eye Structure (1mm Distance from Wave Port)

Figure 5 shows the transmission spectrum versus frequency for the bull's-eye structure with an aperture diameter of 0.75 mm and a frequency step size of 0.1 GHz.

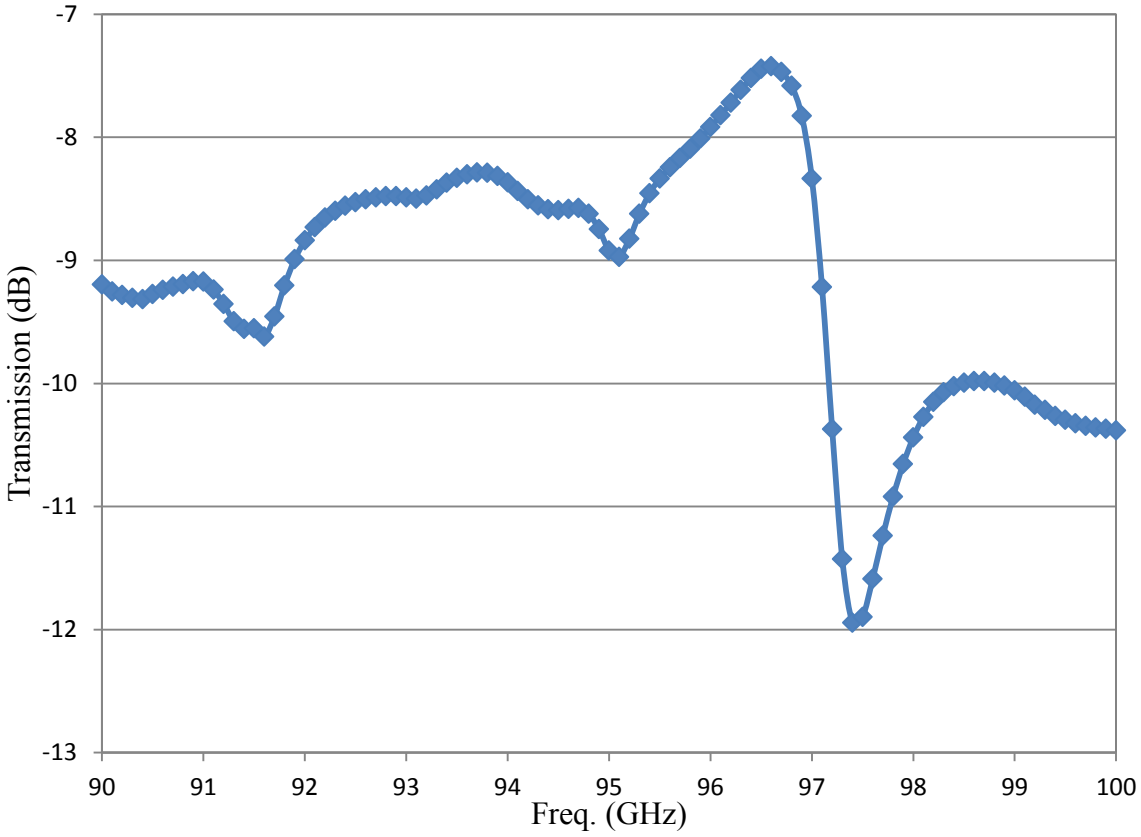

Figure 5. Computed radiation transmission for the 3-mm-wavelength bull's-eye structure (1 mm distance from wave port).

In Figure 5, the radiation transmission peak is at 96.6 GHz, which has exactly 15 times longer wavelength than 1.449 THz-the resonant frequency for the bull's-eye structure designed by Ishihara et al. (2006). This is gratifying because the other dimensions used in this structure design are a 15-times scaling of the Ishihara et al. (2006) design. The radiation transmission is relatively high in the whole frequency range, and minimum transmission occurs just above 97 GHz [1].

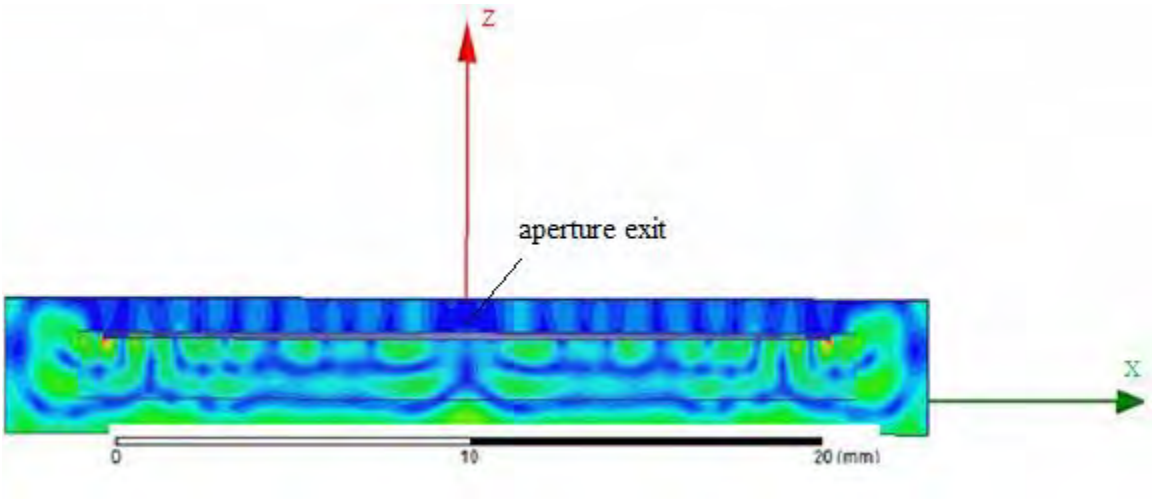

Figure 6. Computed E-field magnitude distribution on the x-z plane of the 3-mm-wavelength bull's-eye structure (1 mm distance from wave port).

Figure 6 shows the electric field magnitude on both sides of the aperture. The red color shows the highest E-field magnitude and the blue color shows the lowest E-field magnitude. As shown in Figure 6, there is no E-field concentration at the aperture exit. This was surprising because the main reason for designing the bull's-eye structure is to have an enhanced E-field at the aperture exit. Although the transmission spectrum seems to be compatible with the Ishihara et al. (2006) results, the E-field is inconsistent. So the transmission spectrum was computed at two other distances: 0.5 mm and 3 mm. 0.5 mm distance was chosen because it is located in the near-field region of the bull's-eye structure, and 3 mm was chosen because it is one wavelength away from the bull's-eye structure, approaching the far-field [1].

3.3.3 3-mm-Wavelength Bull's-Eye Structure (0.5 mm Distance from Wave Port)

Figure 7 shows the transmission spectrum versus frequency of the bull's-eye structure in the near-field region with a frequency step size of 0.5 GHz.

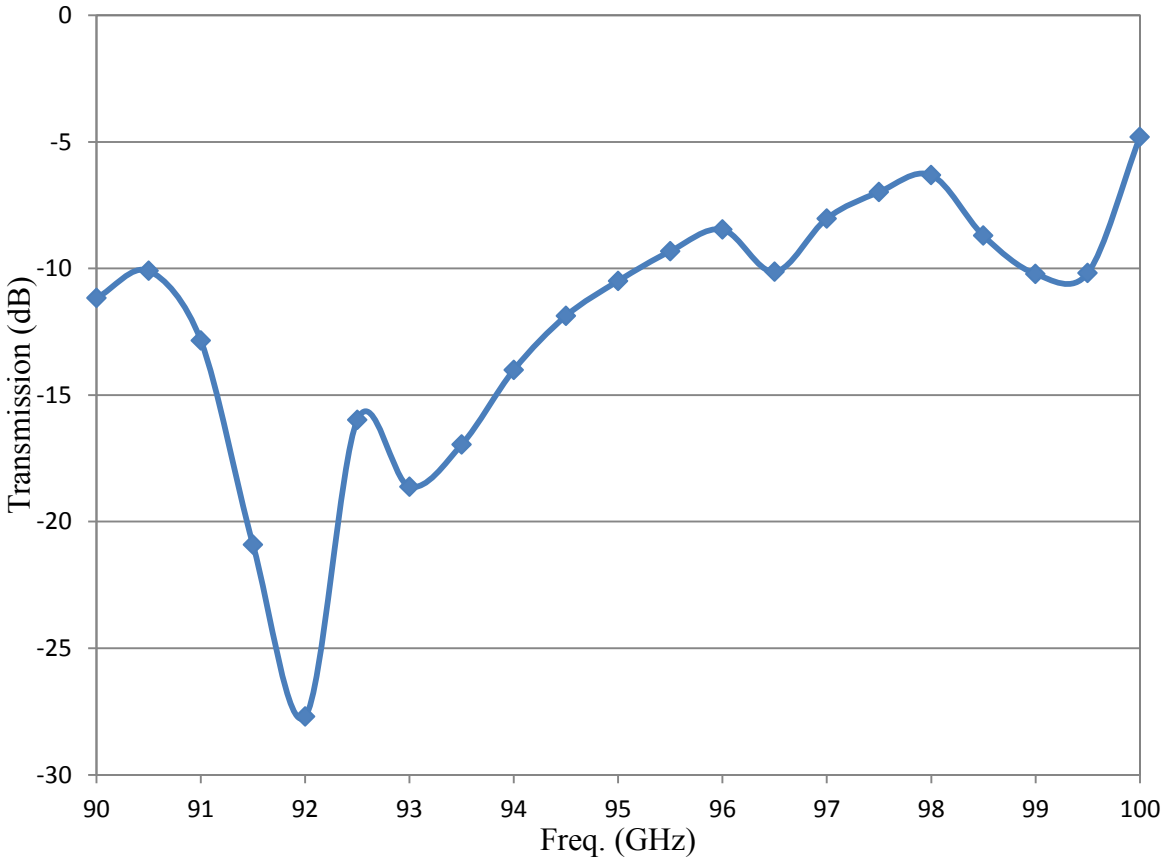

Figure 7. Computed radiation transmission for the 3-mm-wavelength bull's-eye structure (0.5 mm distance from wave port).

The transmission spectrum in Figure 7 is different from the one shown in Figure 5. For instance, the radiation transmission peak is at 100 GHz in Figure 7. Furthermore, the radiation transmission in Figure 7 is very low at 92 GHz, much less than the

minimum in Figure 5. The evanescent waves could be responsible for the difference in the results because they are stronger in the near-field region of the structure.

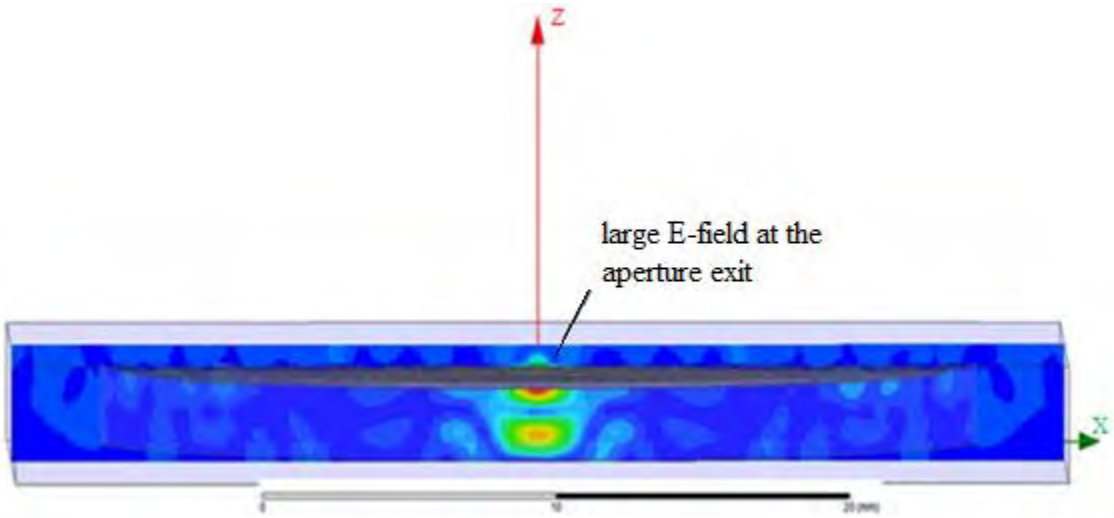

Figure 8. Computed E-field magnitude distribution on the x-z plane of the 3-mm-wavelength bull's-eye structure (0.5 mm distance from wave port).

Figure 8 shows the E-field distribution of the bull's-eye structure as well as the large E-field at the aperture exit. It can be observed that E-field magnitude is extremely large exactly below the aperture exit, which is depicted in red color, and should be caused by the concentration of the surface waves at the center of the structure. In addition, the E-field spot size at the aperture exit is very small, which can show that the enhanced radiation of the bull's-eye structure is a near-field effect, and cannot be observed at the large distances from the bull's-eye structure.

3.3.4 3-mm-Wavelength Bull's-Eye Structure (3 mm Distance from Wave Port)

Figure 9 shows the bull's-eye structure transmission spectrum versus frequency with a frequency step size of 0.5 GHz at approximately one wavelength away from the bull's-eye.

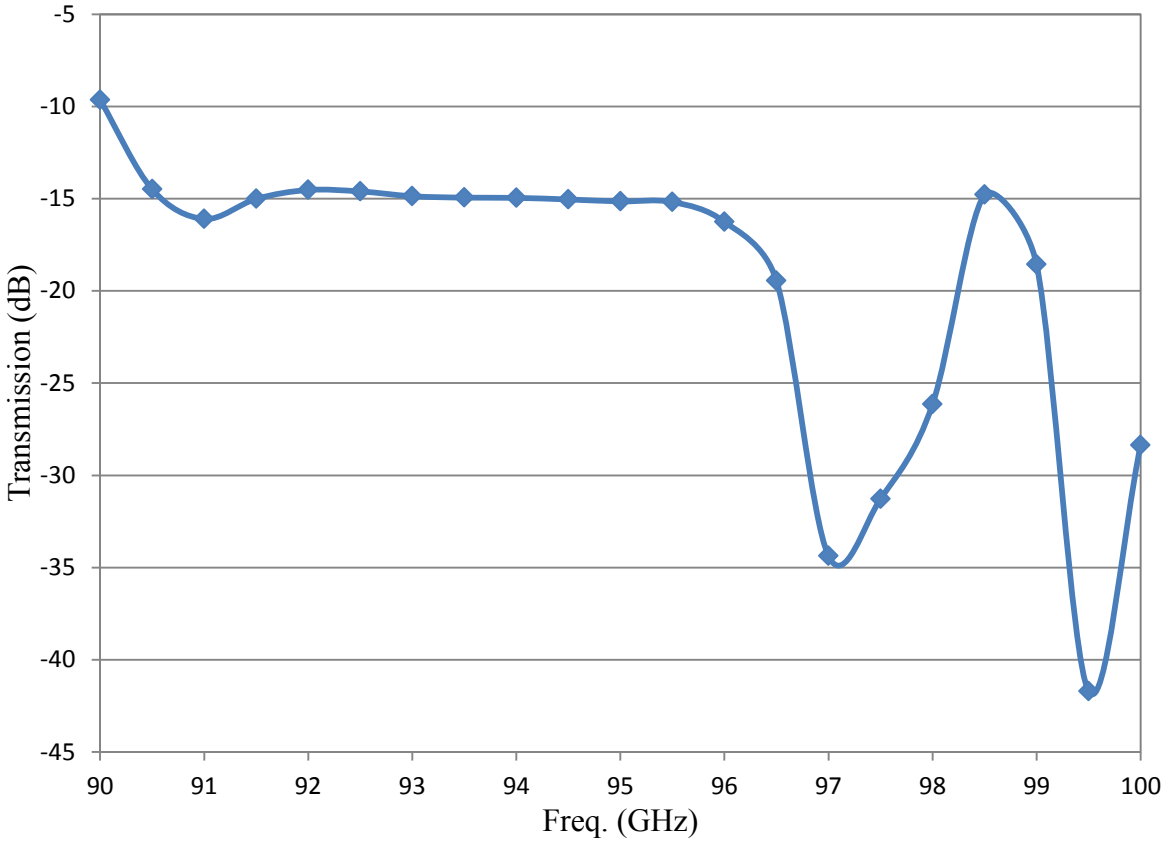

Figure 9. Computed radiation transmission for the 3-mm-wavelength bull's-eye structure (3 mm distance from wave port).

The transmission spectrum in Figure 9 looks much different than the two previous spectra at 0.5 mm and 1 mm distances. It is quite constant in the 91-96 GHz frequency range but is very low near 97 GHz and 99.5 GHz. Also, it should be mentioned that the

radiation transmission has decreased significantly compared to the two other distances. This suggests that the enhanced radiation transmission of the bull's-eye structure is a near-field phenomenon, which is mainly due to the evanescent waves. As a result, when the radiation transmission is computed at a large distance away, a considerable drop in the transmission is observed. It is also worth summarizing that the computed transmission spectra of the bull's-eye structure at the three different distances are not similar and have radiation transmission peaks at different frequencies.

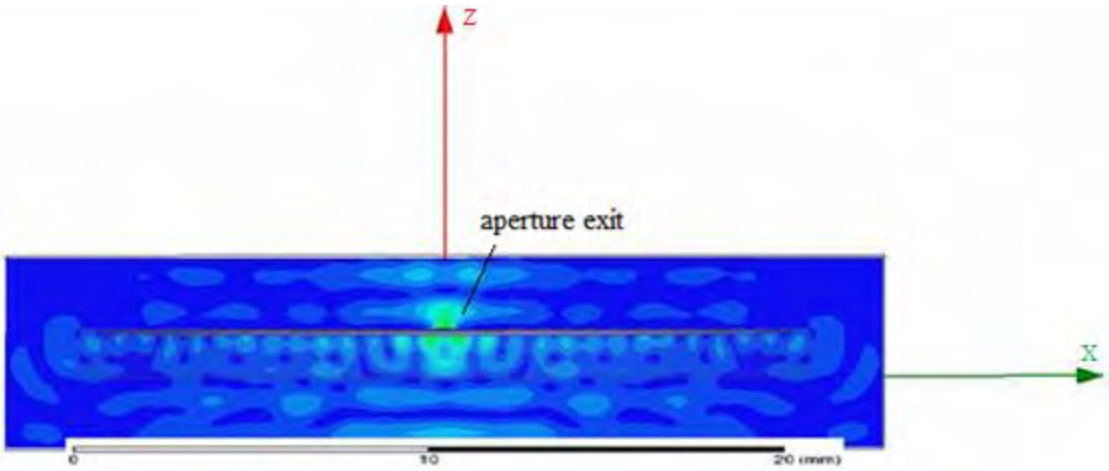

Figure 10. Computed E-field magnitude distribution on the x-z plane of the 3-mm-wavelength bull's-eye structure (3 mm distance from wave port).

In Figure 10, it can be observed that the E-field is large below and at the exit of the aperture. Also, the E-field spot size at the aperture exit in Figure 10 is larger than the one, which is shown in Figure 8.

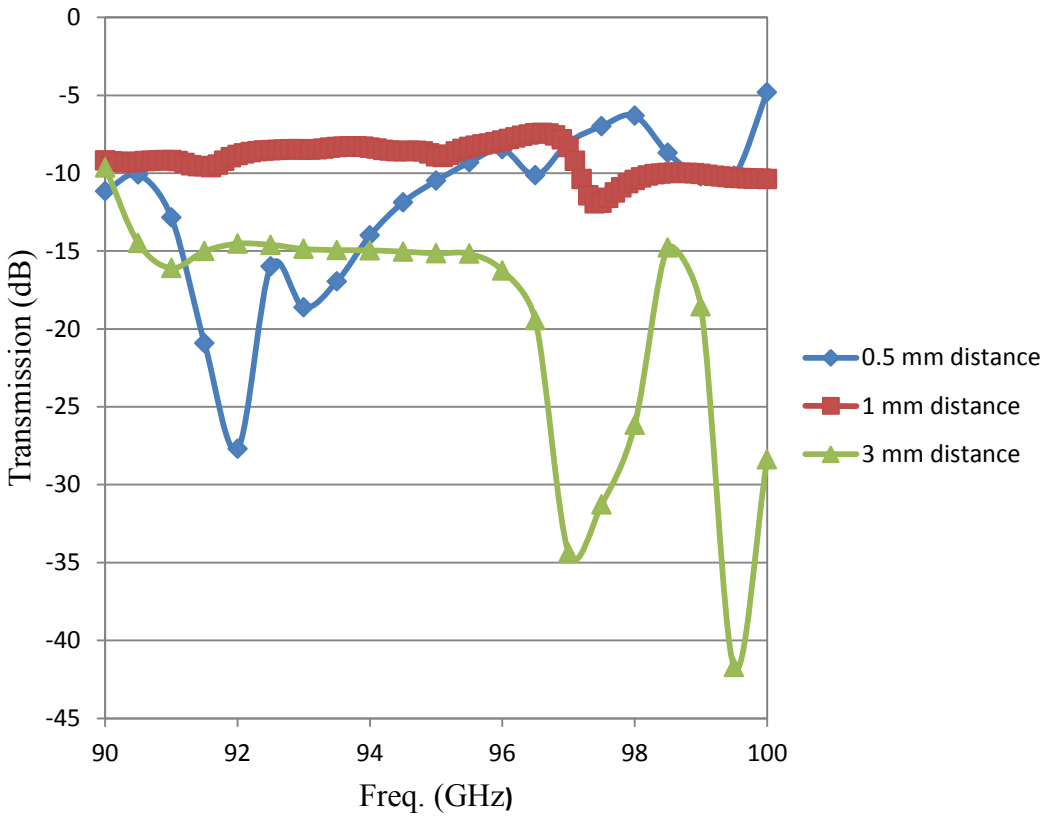

Figure 11. Comparison of computed transmission spectra for 3-mm-wavelength bull's-eye structure at three different distances.

Figure 11 shows computed radiation transmission spectra for the bull's-eye at three different distances. Computed transmission spectra in Figure 11 are different from each other. It can be observed that input-output coupling increased as wave port distance decreased. That was explained in terms of evanescent waves. This explanation can be correct because HFSS radiation ports can couple to evanescent waves. So, when wave ports are at a large distance away from the structure, evanescent waves die out and do not reach the ports [19].

3.4 Sub-Wavelength Circular Aperture without Bull's-Eye Structure (0.5 mm Distance from Wave Port)

Figure 12 shows the sub-wavelength circular aperture with a diameter of 0.75 mm placed in the silver film that covers the Teflon substrate.

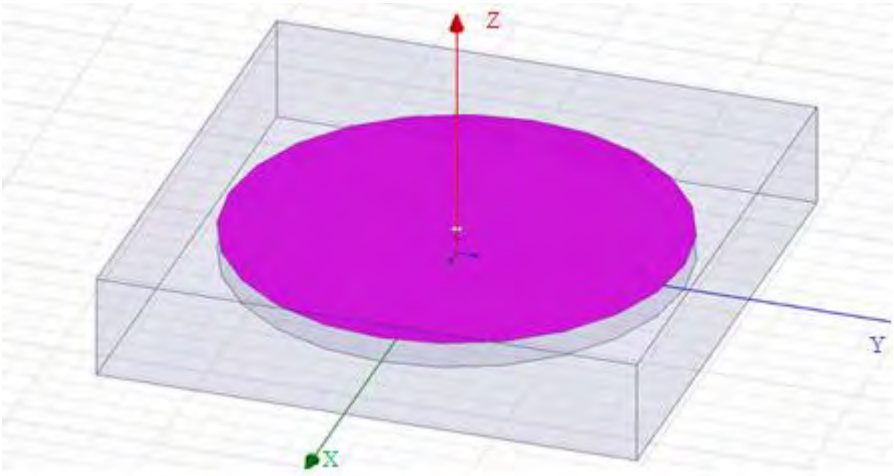

Figure 12. Sub-wavelength circular aperture in the silver film on the Teflon substrate.

The silver film for this design has the same thickness as the bull's-eye structure silver film, and also the Teflon substrate for this design has the same diameter as the designed 3-mm-wavelength bull's-eye structure substrate.

Table 5. Sub-wavelength circular aperture without the bull's-eye structure parameters.

Frequency sweep	90 -100 GHz
Width of grooves	-
Periodicity of grooves	-
Depth of grooves	-
Thickness of silver film	1 μm
Diameter of aperture	0.75 mm
Refractive index of substrate	Teflon, n = 1.45 ($\varepsilon_r = 2.1$)
Angle of incident wave	Normal, from the substrate side

The goal is to compare the bull's-eye structure radiation transmission to the sub-wavelength circular aperture radiation transmission. This is important to determine how much the bull's-eye structure improves the radiation transmission compared to the sub-wavelength circular aperture without a periodic structure. The sub-wavelength circular aperture parameters are also summarized in Table 5. The radiation transmission was computed at the distance of 0.5 mm from the circular aperture to compare the transmission values in the near-field region.

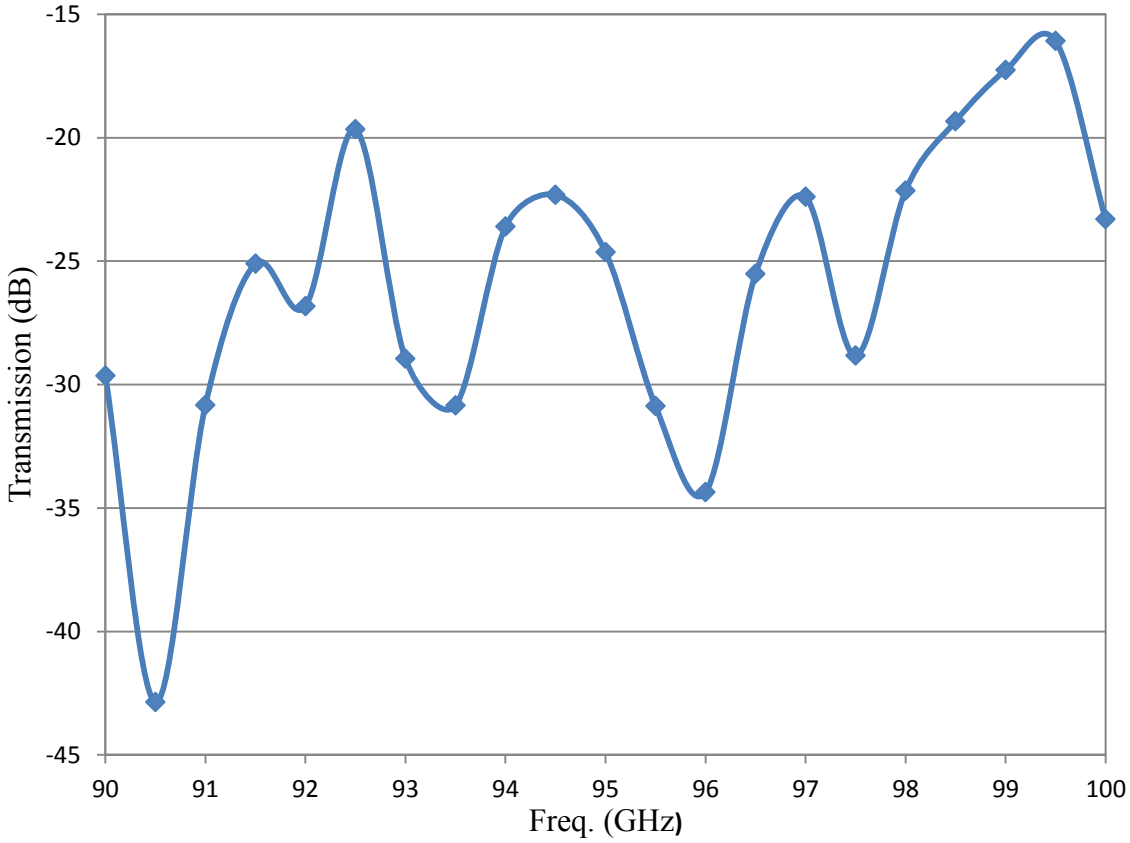

Figure 13. Computed radiation transmission for the sub-wavelength circular aperture without periodic structure (0.5 mm distance from wave port).

Figure 13 shows the radiation transmission of the sub-wavelength circular aperture in the silver film on the Teflon substrate. The highest radiation transmission is close to -15 dB at 99.5 GHz, and the lowest radiation transmission is less than -40 dB. In addition, the transmission spectrum shows large variation in the 90-100 GHz frequency range.

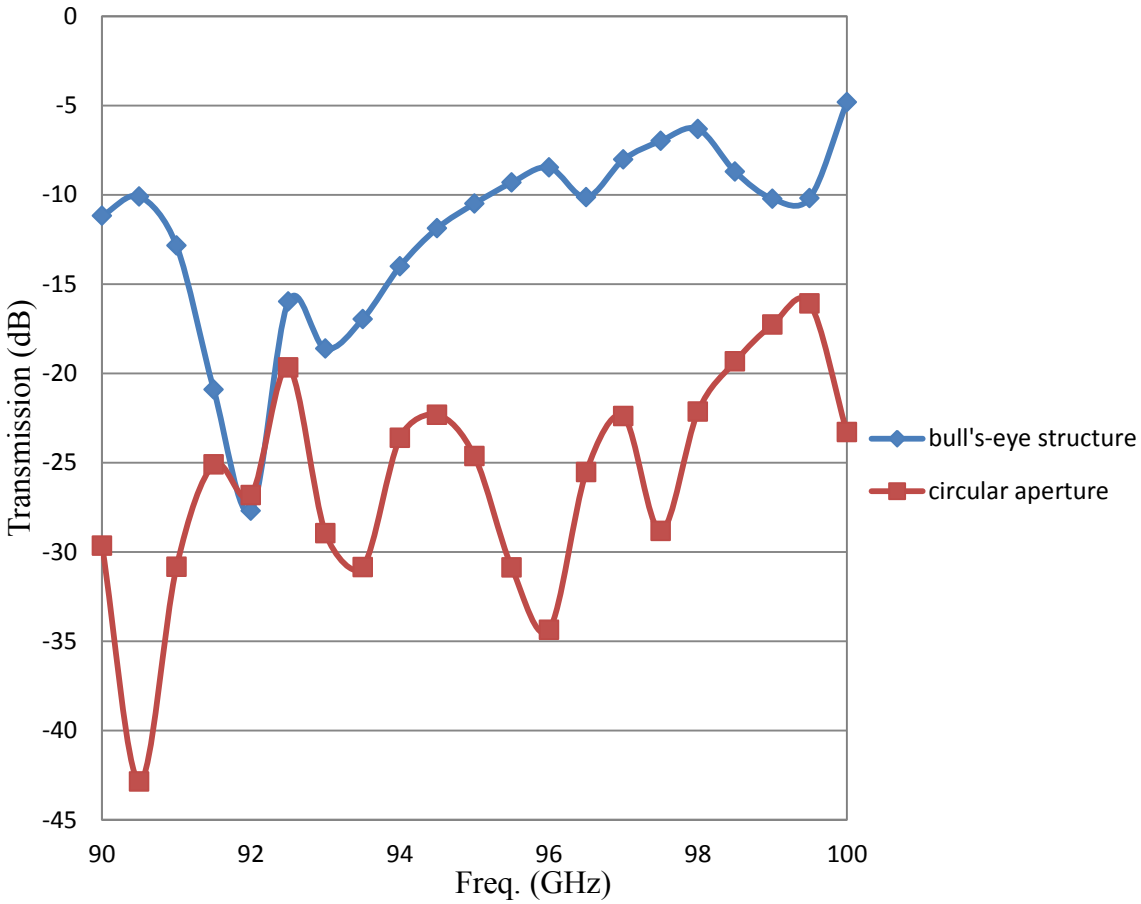

Figure 14. Radiation transmission comparison of the sub-wavelength circular aperture with and without bull's-eye structure in the near-field region.

Figure 14 shows the comparison between the circular aperture and bull's-eye structure clearly. The radiation transmission is improved by using concentric, periodic grooves around the sub-wavelength circular aperture. The bull's-eye structure radiation transmission is much higher than the circular aperture except at the frequencies close to 92 GHz, which is not good because the purpose of designing the bull's-eye structure is to improve the radiation transmission of the sub-wavelength aperture.

3.5 500 GHz Bull's-Eye Structure

In the interest of using the bull's-eye structure for bio spectroscopy, a structure was designed to perform at 500 GHz. The dimensions of this bull's-eye structure are approximately one-fifth of those used in the 3-mm-wavelength design. Transmission spectrum was computed at 200 μm (~λ/3) distance from the bull's-eye structure.

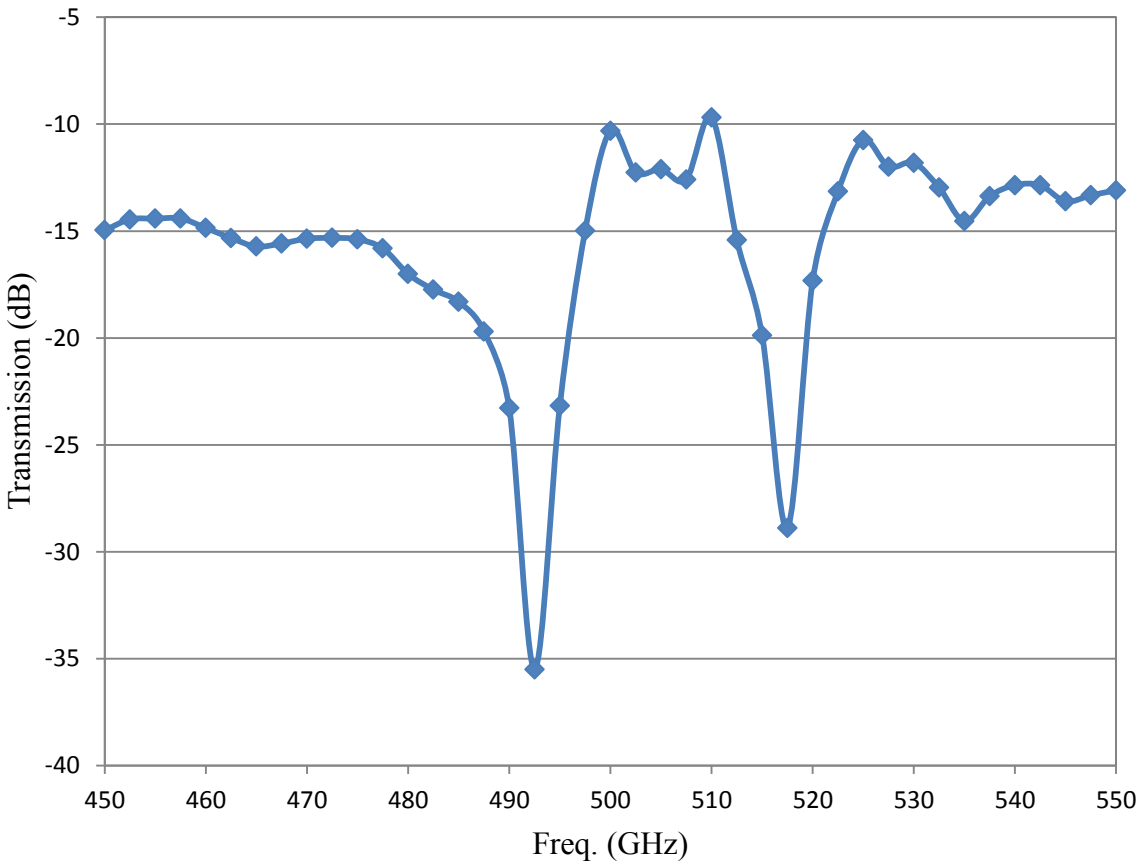

Figure 15. Computed radiation transmission of 500 GHz bull's-eye structure.

Figure 15 shows that the radiation transmission is quite high at 500 GHz and is close to -10 dB. Also, the radiation transmission is high in the frequency range of 495-510 GHz. The dimensions of this designed bull's-eye structure are approximately a three-

times scaling of Ishihara et al. (2006) design and Figure 15 shows that these dimensions are the proper values for the 500 GHz bull's-eye structure design because high radiation transmission is observed at the design frequency [1].

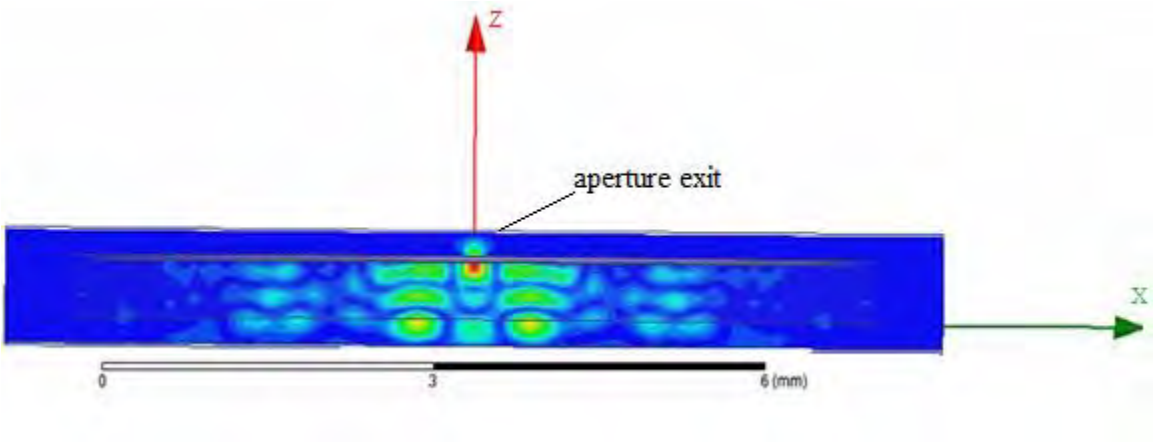

Figure 16. Computed E-field magnitude distribution on the x-z plane of the 500 GHz bull's-eye structure.

Figure 16 shows the E-field magnitude at the aperture exit. The E-field is extremely large at the center of the bull's-eye structure below the aperture because of the radial concentration of the surface waves. In addition, the E-field spot size at the aperture exit is relatively small.

3.6 Fabrication of 3-mm-Wavelength Bull's-Eye Structure

The periodic grooves in the 3-mm-wavelength bull's-eye structure were created with a CNC lathe on a Teflon or high-density polyethylene (HDPE) substrate. Both of these substrate materials are transparent in the THz region. Also, they are readily available materials, and have good machining properties. After the CNC machining was

complete, the corrugated substrate was separated from the Teflon rod. A Silver film having 1 μm thickness was deposited on the substrate by thermal evaporation. Then the central circular aperture was made in the silver film using a 0.75 mm drill bit.

The thickness of the silver film was determined by the requirement that it should be large enough to prevent radiation from transmitting through it.

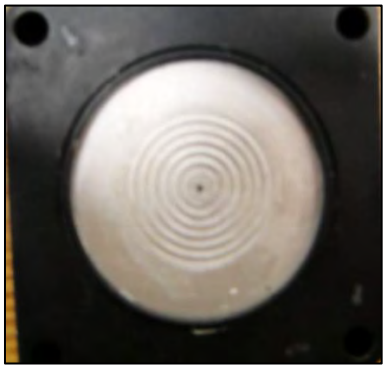

Figure 17. Fabricated bull's-eye structure with six periodic grooves covered with the silver film.

Figure 17 depicts the fabricated bull's-eye structure with a sub-wavelength circular aperture. An experiment was needed to determine the spatial resolution of the structure, which is discussed next.

4. Experimental Measurement

4.1 Spatial Resolution Measurement Method

The quality of the fabricated 3-mm-wavelength bull's-eye structure was determined by measuring its spatial resolution. This was done using the knife-edge resolution technique, and this technique is defined as the lateral displacement of a sharp knife edge so that 90% to 10% of the transmitted signal strength is allowed through an aperture [5].

4.2 Knife-Edge Test

A knife-edge test was conducted to measure the spatial resolution of the bull's-eye structure by moving a sharp knife edge across the circular aperture of the bull's-eye structure. The spatial resolution was measured was measured in two directions (X-axis and Y-axis).

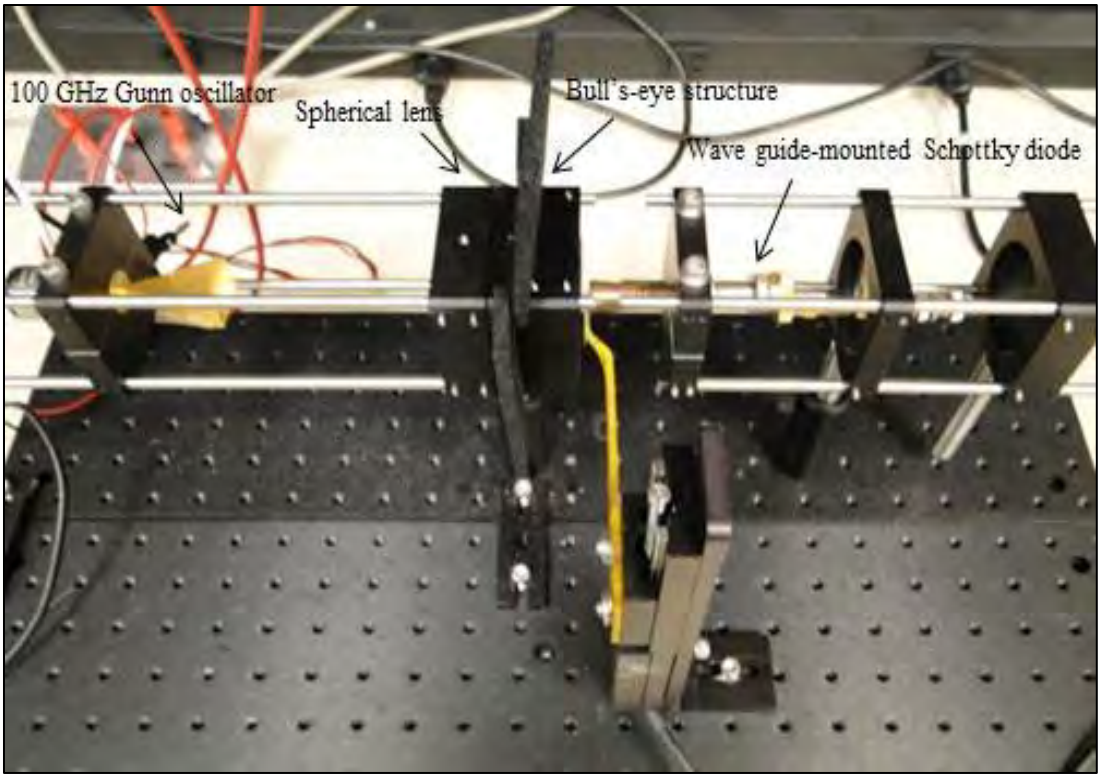

Figure 18. Knife-edge test set up for measuring the bull's-eye structure spatial resolution.

For this test, the radiative source is a 100 GHz voltage-controlled Gunn oscillator with the pyramidal feed horn. The polarization of the Gunn oscillator was in the vertical direction (Y-axis). The source was chopped at 100 KHz, and the radiation was transmitted through a spherical lens with the bull's-eye structure pointed toward the wave guide-mounted Schottky-diode detector. The detector's wave guide was a corrugated conical feed horn. The corrugation of the conical feed horn reduces the side lobes.

A spherical lens was used behind the bull's-eye structure to collimate the Gaussian beam of the source. Therefore, there is much less radiation leakage around the sides of the lens, and the majority of the radiation detected is the radiation that is transmitted through the bull's-eye structure. The substrate side of the bull's-eye structure

faces the source, and the wave is normally incident on this side. The detector is placed at the closest possible distance from the aperture (~2 mm) because the bull's-eye structure radiation transmission is high in the near-field region.

4.3 Results of the Knife-Edge Test: Spatial Resolution Curves

By using the knife-edge resolution definition, the spatial resolution can be measured along the X and Y axes from the measured transmission curves.

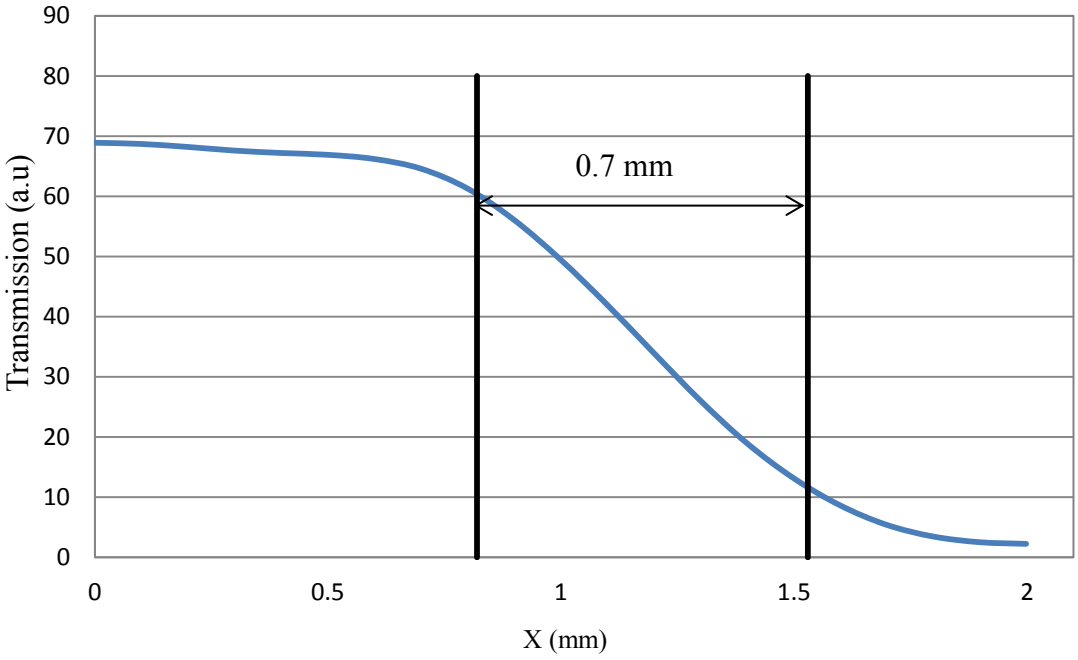

Figure 19. Measured spatial resolution curve along the X-axis.

The spatial resolution curve along the X-axis is shown in Figure 19. The signal is approximately constant out to X = 0.6 mm and has its highest strength near X = 0, as expected. When the knife edge starts moving across the aperture, there is a sharp drop in the signal strength until the knife edge covers the aperture completely. Then the signal

strength goes approximately to zero. Based on the definition of the knife-edge resolution, Figure 19 shows that the knife edge displacement from 90% to 10% of the signal strength is approximately 0.7 mm. This means that the spatial resolution was 0.7 mm along the X-axis, which is approximately λ/4 at 100 GHz (3 mm wavelength).

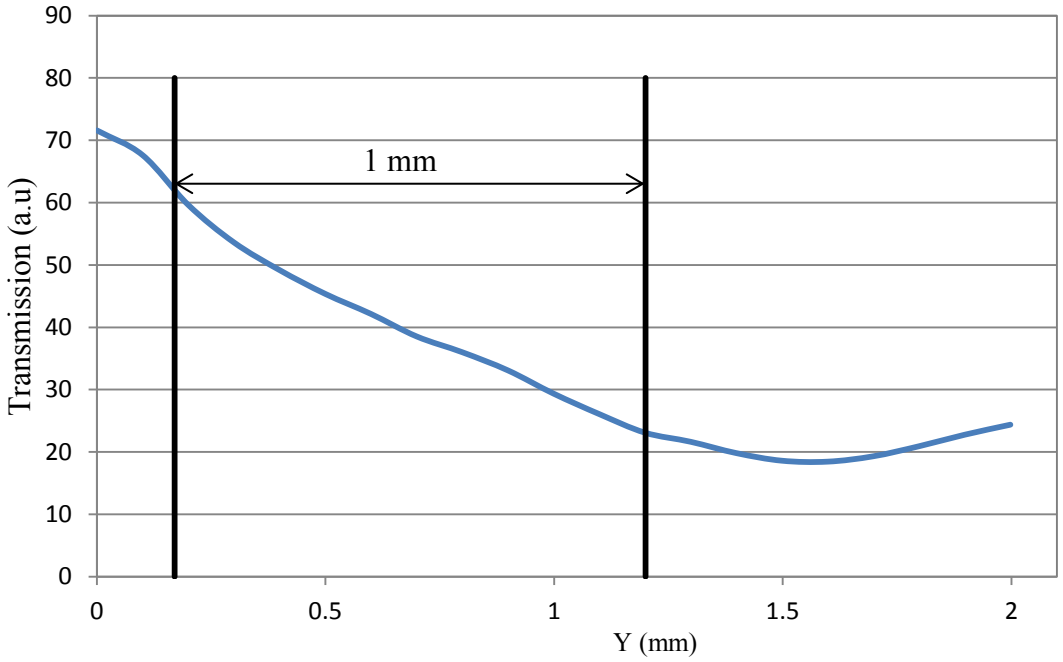

Figure 20. Measured spatial resolution curve along the Y-axis.

The spatial resolution curve along the Y-axis was not as well behaved as along the X-axis. There are two differences in Figure 20 in comparison to Figure 19. The first one is that there is no initial constant signal strength region in Figure 20 as was seen in Figure 19. The second difference is that the signal strength in Figure 20 does not go to zero even when the knife edge covers the aperture completely; however, one can still observe the sharp drop in the signal strength when the knife edge starts covering the aperture. These

differences could be caused by the leakage around the lens sides. Although the radiation was collimated by using a spherical lens behind the bull's-eye structure and covering the lens holder sides with the absorbers, radiation can still leak around the lens sides.

Moreover, the obtained spatial resolution along the Y-axis is ~1 mm, which is λ/3 at 100 GHz, so the obtained results show that the fabricated bull's-eye structure has ~λ/4 spatial resolution along the X-axis and λ/3 spatial resolution along the Y-axis. However, the fabricated bull's-eye structure probably has the better spatial resolution than this because the detector had to be placed at ~2 mm distance from the bull's-eye structure since the detector was physically large compared to the wavelength of radiation. Because of this, the detector could not be placed less than two millimeters from the bull's-eye structure [5].

Finally, many difficulties were faced and overcome pertaining to the knife-edge test. The first one was a distance of detector from the bull's-eye structure. By bringing the detector to the closest possible distance from bull'-eye, obtained results improved considerably. Other issue was radiation leakage from lens holder sides. The main reason for radiation leakage from lens holder sides was the Gaussian beam shape of wave source radiation, so a spherical lens was used behind the bull's-eye to collimate radiation and reduce leakage of radiation. To have the lowest amount of radiation leakage, lens holder sides were covered with absorbers. Also, a large-area detector was used for the knife-edge experiment. Detector can be placed at a closer distance from bull's-eye if it is physically smaller. It is recommended to use a physically smaller detector in the near-field region of bull's-eye structure for future works because that results in smaller measured spatial resolution.

5. Design and Simulation of the 100 GHz Reflective Probe

5.1 Probe Applications

The water content of cancerous and burnt tissues is often higher than in healthy tissue, so these tissues have higher energy absorption and higher reflectivity compared to healthy tissues in the THz region. This higher energy absorption and reflectivity of these tissues enables their detection by using a reflective probe [20].

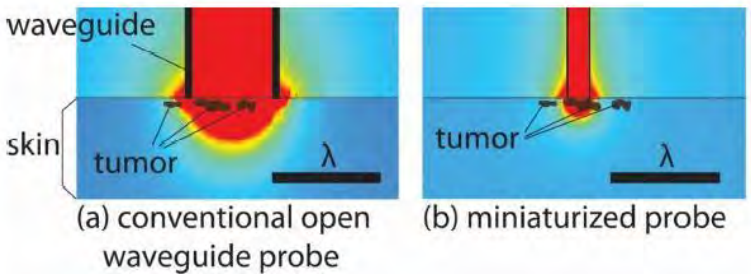

Figure 21. Comparison of interaction volume and spatial resolution of (a) large-tip-sized probe (b) tiny-tip-sized probe [20].

As shown in Figure 21, the conventional open-waveguide probe has a large tip size which results in large spatial resolution and interaction volume. If one wants to detect small features such as skin-cancer tissues at an early stage, the conventional probe will not have enough spatial resolution for positive detection. Thus, a probe with a smaller tip size should be used [20].

5.2 Design and Simulation of the Reflective Probe

The purpose, to design a reflective probe, is to use the probe for skin-burn and skin-cancer tissue detection. The baseline design has a square-shaped tip with 0.4 mm^2 (625 * 10^{-6} in^2) area. The tiny tip size will have good special resolution for cancerous and burnt tissue detection. The probe is constructed from silicon which has a high relative permittivity (ε_r = 11.9). This helps for better E-field concentration in the probe. Simulations were conducted on the designed reflective probe in HFSS. As shown in Figure 23, the designed near-field probe has a reflection of equal to the -10.52 dB at 100 GHz.

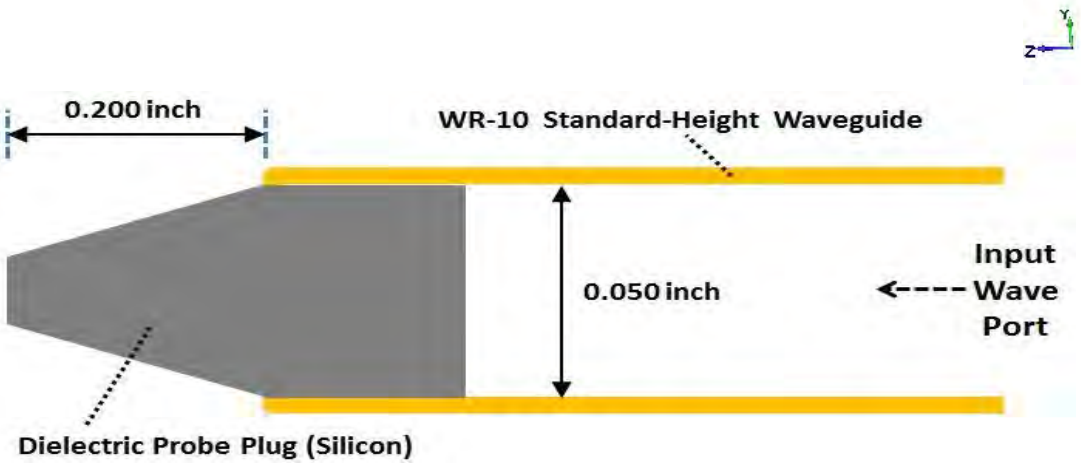

Figure 22. Designed 100 GHz reflective probe.

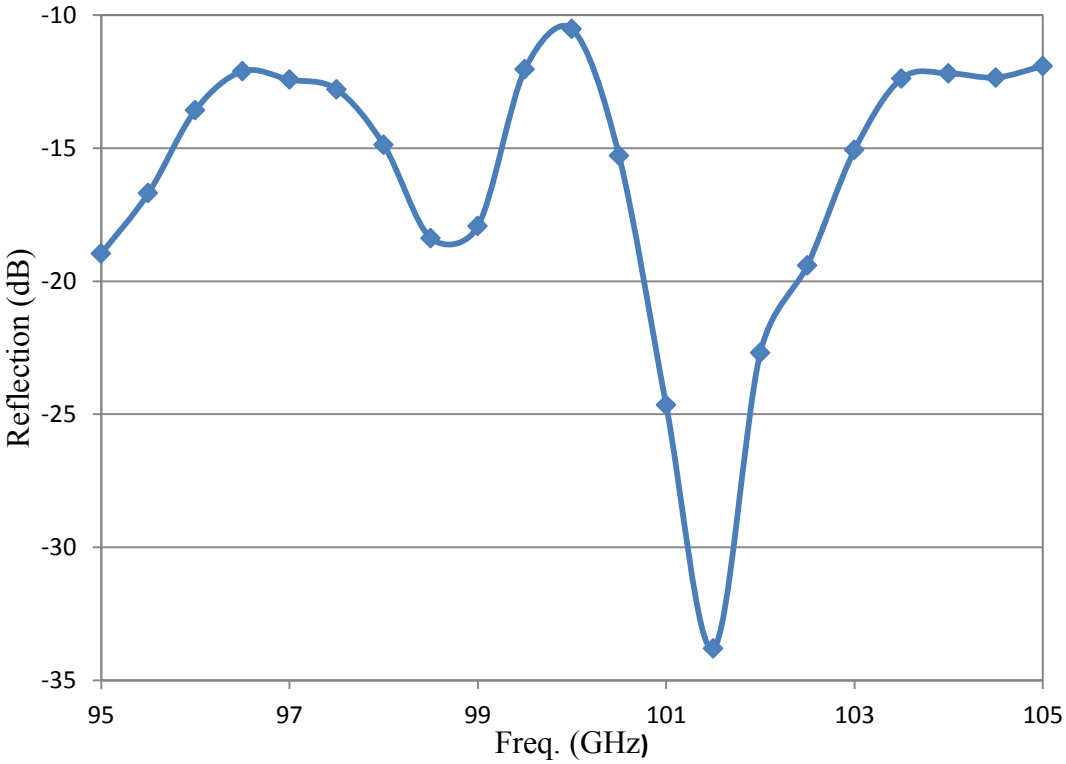

Figure 23. Reflection spectrum of the designed probe.

As shown in Figure 23, the silicon reflective probe has a reflection peak at the design frequency of 100 GHz and also in the frequency ranges of 103-105 GHz and 96-97 GHz. Except for the frequencies close to 101 GHz, the reflection is usefully high in the 95-105 GHz frequency range.

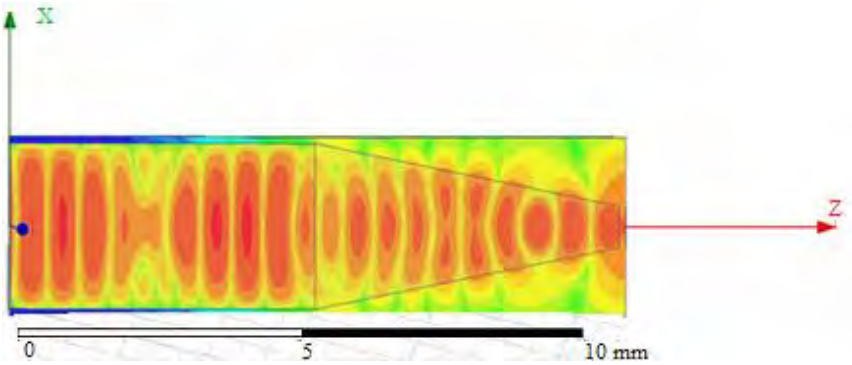

Figure 24. Computed E-field magnitude distribution on the x-z plane of the probe at 100 GHz (polarization direction is along the Y-axis).

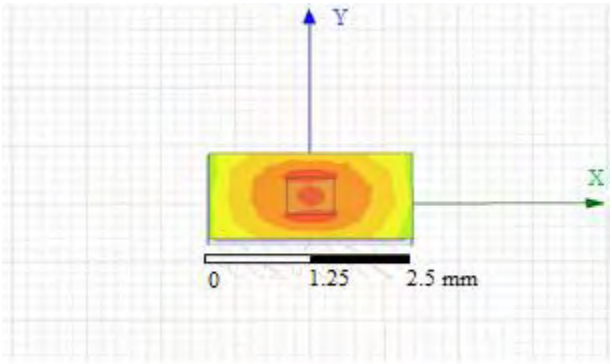

Figure 25. Computed E-field magnitude distribution on the x-y plane of the probe at 100 GHz, 1 μm away from the probe tip.

Figures 24-25 show the E-field magnitude distribution of the probe in two different planes. The wave propagation can be observed in the probe in Figure 24. Figure 24 also shows a highly concentrated E-field in the probe because it is constructed from silicon. For instance, if the probe would be constructed from Teflon, such high E-field magnitude distribution in the probe could not be observed. Figure 25 shows that the E-field concentrates at the probe tip with the small spatial resolution.

6. Conclusion

A bull's-eye structure with a sub-wavelength circular aperture was designed to perform at a wavelength of ~3 mm in W band (75-110 GHz). This bull's-eye structure can be used for skin-tissue detection, such as detecting melanoma. Simulations were carried out on the 3D model of the bull's-eye structure in HFSS. The simulation results show the computed transmission spectra for the designed bull's-eye structure. The transmission spectrum was computed for a 3-mm-wavelength bull's-eye structure at three different distances (0.5 mm, 1 mm, and 3mm). The three computed transmission spectra were different from each other, and a considerable drop in the computed radiation transmission magnitude was observed at the distance of 3 mm compared to that computed at the other two distances. This is because the enhanced radiation transmission of the bull's-eye structure is a near-field effect.

A 3-mm-wavelength bull's-eye structure was fabricated and measured for its spatial resolution by the knife-edge test. The detector was placed at the ~2 mm distance from the bull's-eye structure. By conducting the knife-edge test at 100 GHz, a resolution of 0.7 mm (~$\lambda/4$) was obtained along the X-axis and 1 mm was obtained along the Y-axis. The difference in the obtained spatial resolution results can be because of the radiation leakage around the lens sides. Also, the detector was physically large compared to the radiation wavelength, so a better resolution would likely have been obtained if a smaller detector was used in near-field region of the bull's-eye structure.

Also, a bull's-eye structure with a sub-wavelength circular aperture was designed to have resonant frequency of at least 500 GHz. This bull's-eye structure can be used in biological sensing and detection. Then the 3D model of the 500 GHz bull's-eye structure was simulated in HFSS. The obtained transmission spectrum for the 500 GHz bull's-eye structure shows that the designed bull's-eye structure has high radiation transmission in the 500-510 GHz frequency range.

Finally a silicon reflective probe was designed to perform at 100 GHz. The design probe had a tiny tip with an area of 0.4 mm^2. This probe with a tiny tip can be used for detection of small features such as skin burn and melanoma. The probe was constructed from silicon because it has high relative permittivity and concentrates the E-field in the probe. The obtained results from the simulation of the reflective probe in HFSS show that the probe has high reflection at 100 GHz. Also, the E-field at the probe tip has large magnitude and small spot size.

Appendix I. BobCAD-CAM Job Creation

Introduction

BobCAD-CAM is a software tool for designing 3D parts and creating G-code for CNC fabrication. The main advantage of using BobCAD is that it allows importing CAD files designed with other software, such as SolidWorks and AutoCAD. BobCAD is mainly used for programming G-code for CNC lathe and milling machines [21].

Milling

BobCAD-CAM can be used for 2- and 3-axis milling operations where it provides a user with a large number of operations for programming G-code for complicated geometries. For example, engraving, profiling, pocketing, and plunge roughing are possible milling operations, and can be done with control of several other machining parameters, such as stock geometry, milling tool data, cutting feed rate, and plunge feed rate [21].

Lathe

The lathe is used for manufacturing a part which is axisymmetric. For parts to be cut on the lathe and designed in BobCAD, it is required to draw the 2D cross section (profile) of the part in the top left quadrant of drawing plane. However, BobCAD does not have the ability to import data points for these profiles. Instead, SolidWorks can be

used for importing such data points. The profile is simply drawn in SolidWorks and can be extruded along its normal vector to become the 3D part because BobCAD cannot import 2D parts drawn in SolidWorks. Then the edge of the 3D part can be extracted with a function in BobCAD to obtain the 2D profile. For more information regarding lathe drawing, one can watch the training videos available in the THz sensors group dropbox folder [22, 23].

Post-Processor

The format of G-code produced by BobCAD is controlled by a post processor, and different CNC machines have different controllers. In order to have the right G-code format for a specific controller, the correct post-processor should be used. The updated post-processors can be downloaded directly from the BobCAD website. Both CNC machines in the THz sensors group have Mach 3 controllers, and the updated Mach 3 post-processors can be downloaded from the BobCAD website [22, 23, 24].

To produce G-code in BobCAD for running a CNC machine, there are several steps which should be taken. First, a part is designed in BobCAD. Then a set of operations is selected for fabricating the part. After that, the G-code is posted in BobCAD and saved for running the appropriate CNC machine. As an example of the different steps required to program G-code for a desired geometry, the 3-mm-wavelength bull's-eye fabrication procedure in BobCAD is explained.

Bull's-Eye Structure Design in BobCAD

The bull's-eye structure is an axisymmetric geometry, so it can be fabricated by a CNC lathe. Figure 26 (far right) shows the cross section of the bull's-eye structure with six periodic grooves. By clicking on "Preferences" in Figure 26, "Settings Part" can be selected [23, 24].

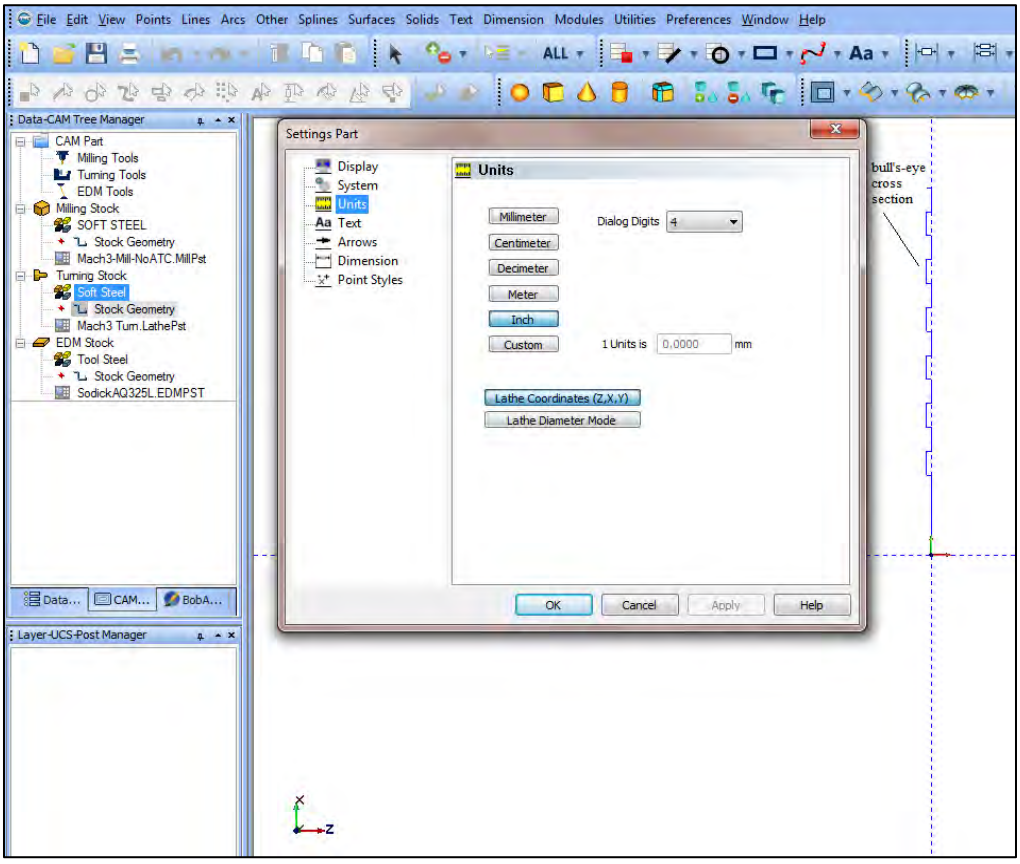

Figure 26. Setting "Units" and turning on "Lathe Coordinates".

As shown in Figure 26, "Lathe Coordinates (Z, X, Y)" should be selected because lathe axes are different from the milling axes. Z is the axis of symmetry. Then by right clicking on "Turning Stock" and selecting "Edit" in Figure 27, the stock values can be

entered, as shown in Figure 28. In Figure 28, it is not necessary to change "Material" from "Soft Steel" to Teflon because the feed rate and speeds will be set manually for this design (desired values will be entered). The feed rate and speeds will be entered manually because the calculated values by BobCAD are not always the proper values for cutting the intended piece. "Face Z", which shows where the material starts, was set to zero. "Cutoff Z", "End of Stock Z", and "Stock Diameter" values were inserted. "Internal Diameter" was set to zero because there is no hole through the center of the structure. The stock is shown on the screen as the blue cylinder on the right in Figure 28. "Clearance" values can be changed to 0.1 inch for "Face" and "Diameter". "Clearance" shows the distance between the tool tip and the piece before the tool starts cutting the piece [24, 25].

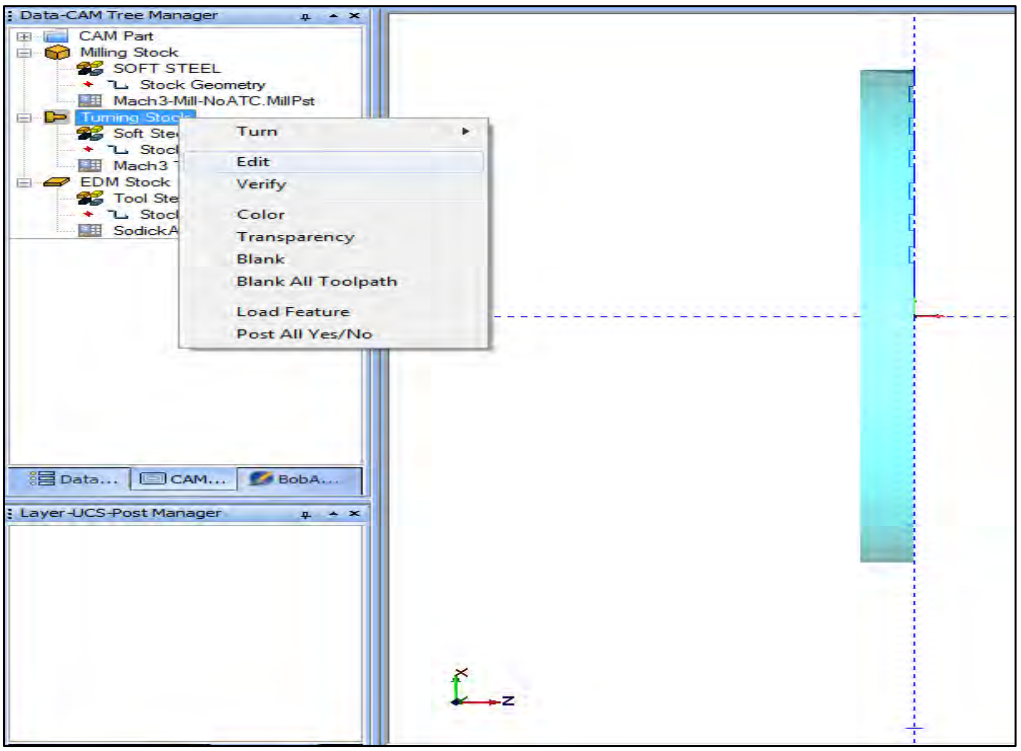

Figure 27. Setting the stock values.

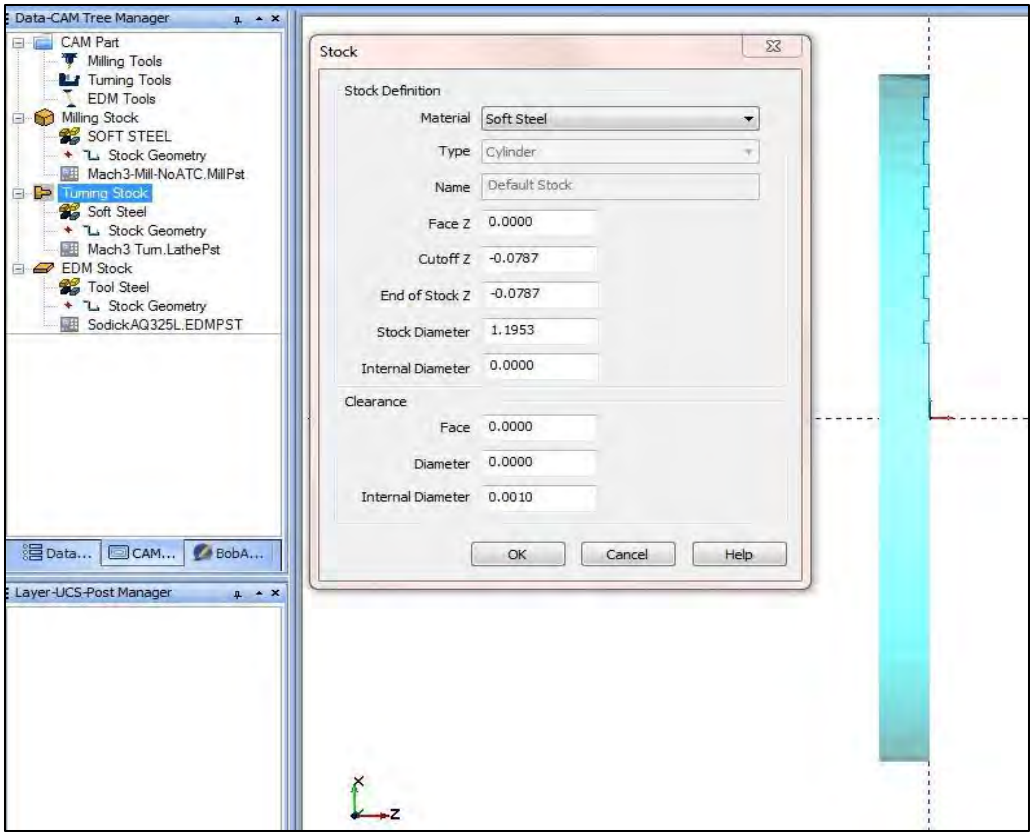

Figure 28. Entering the stock values.

After determining the stock values, one should add a tool path for cutting the bull's-eye structure. As shown in Figure 29, "Rough" operation was selected, and "Feature Rough" is then loaded to the CAM tree and can be observed in Figure 30. By right clicking on "Geometry" in Figure 30, bull's-eye cross section can be selected as the geometry which should be cut. As shown in Figure 30, the selected geometry is highlighted in red color. After selecting "Rough" in the CAM tree, "Canned Cycles" was selected for "Posting Parameters" in Figure 31 because it produces the shortest amount of code. For "Cycle Type", "Turning Rough" was selected. The tool path for "Turning Rough" is also shown in the blue colored lines in Figure 31. "System Compensation" in

Figure 31 was turned off, which gives exactly point-to-point movement of the tool on the model. “Machine Compensation” was turned on to account for movement of the tool tip on the model [23, 24].

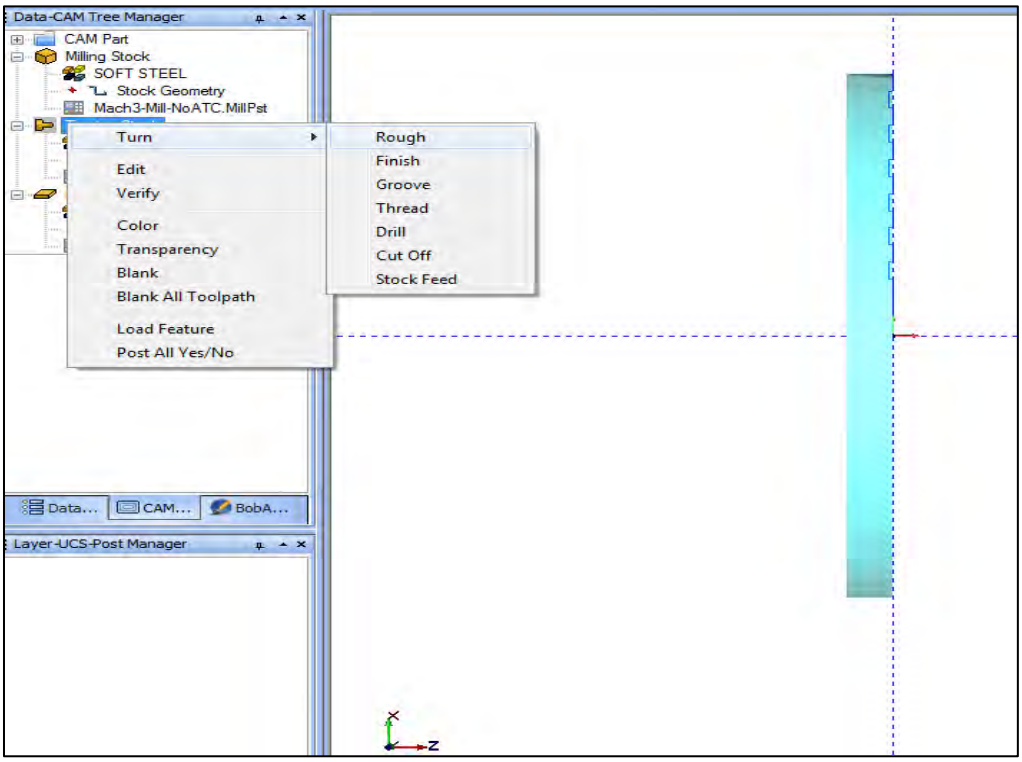

Figure 29. Adding the tool path.

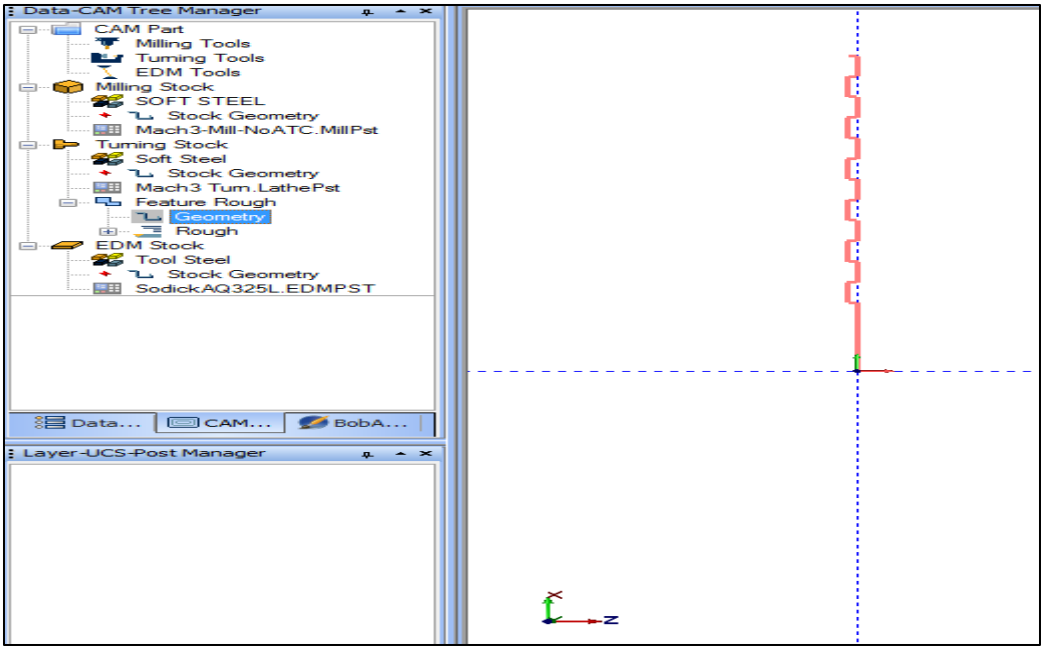

Figure 30. Selecting the geometry.

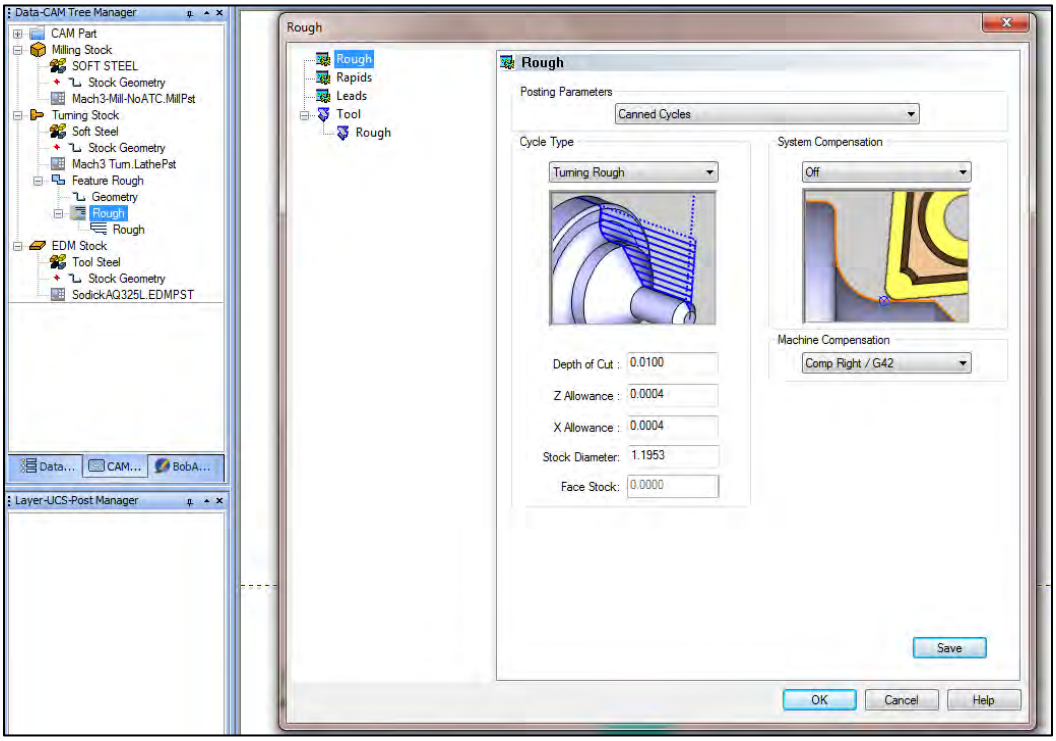

Figure 31. Setting the "Feature Rough".

In Figure 32, the direction that the tool departs the surface of the material is set by “Rapids”. The tool always departs the piece in a proper direction although the departure direction of the tool from the piece can be set manually in “Rapids”. For “Rapids On Exit To Tool Home Z-X” in Figure 32, the tool departs the material surface along the Z-axis to reach the tool home position, and then it moves along the X-axis. The tool home position is a place where the tool goes after the completion of an operation [23, 24].

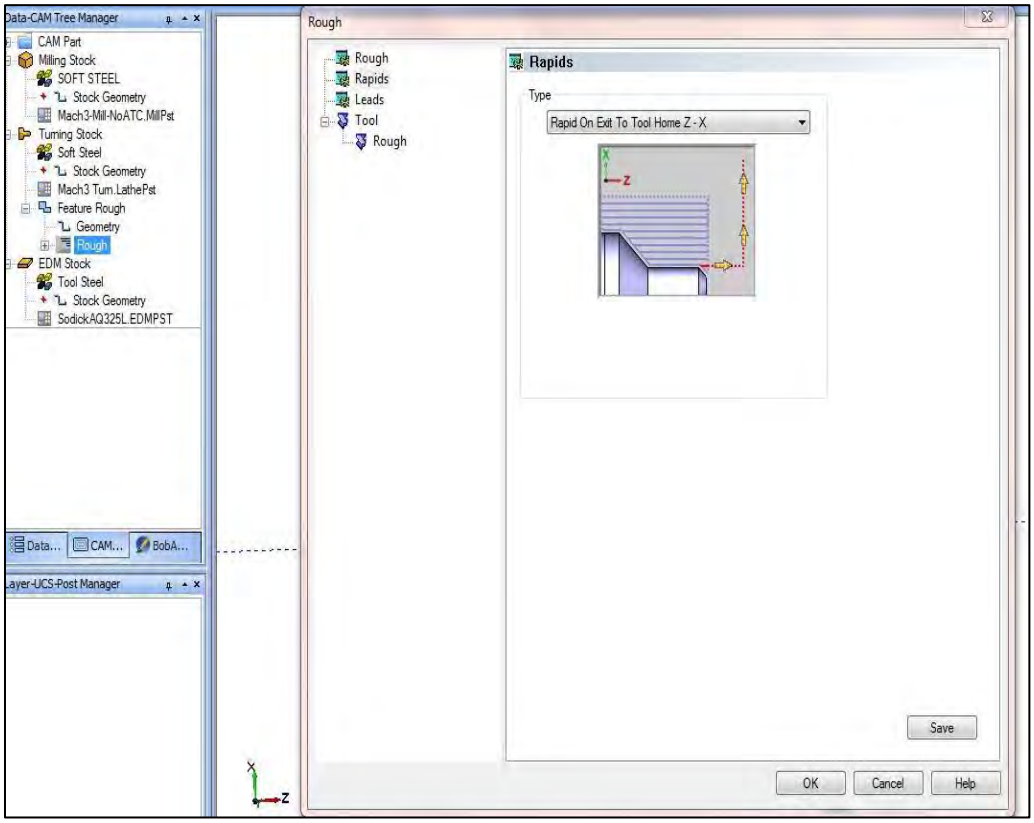

Figure 32. Setting “Rapids”.

The approach and departure of the tool from the piece can be set using “Leads” shown in Figure 33. Both “Leadin” and “Leadout” points can be set. Different tool tip parameters, such as “Noise Radius”, “Tool Angle”, and “Cutting Angle” can also be set,

as shown in Figure 34. When the mentioned tool parameters are set, the theoretical edge of the tool is calculated by Bob CAD ("Theoretical Z" and "Theoretical X"). The shape of tool tip can also be set, such as "Diamond Insert" shown in Figure 34 [23, 24].

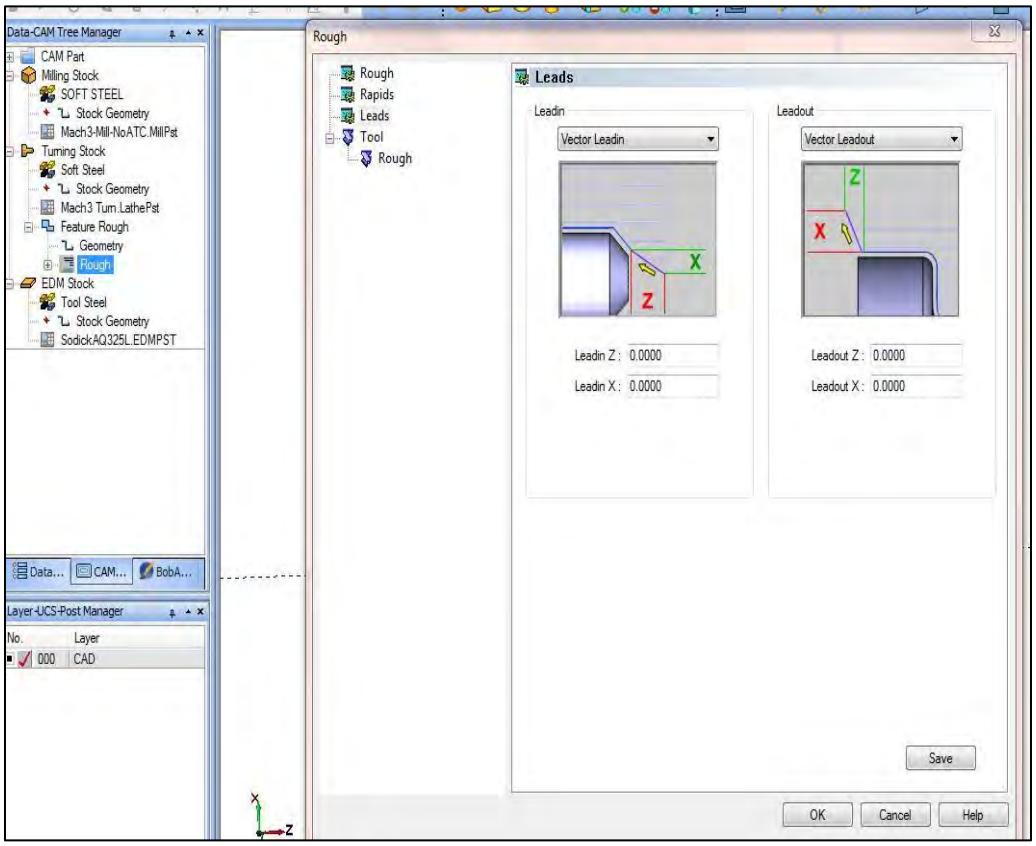

Figure 33. Setting "Leads".

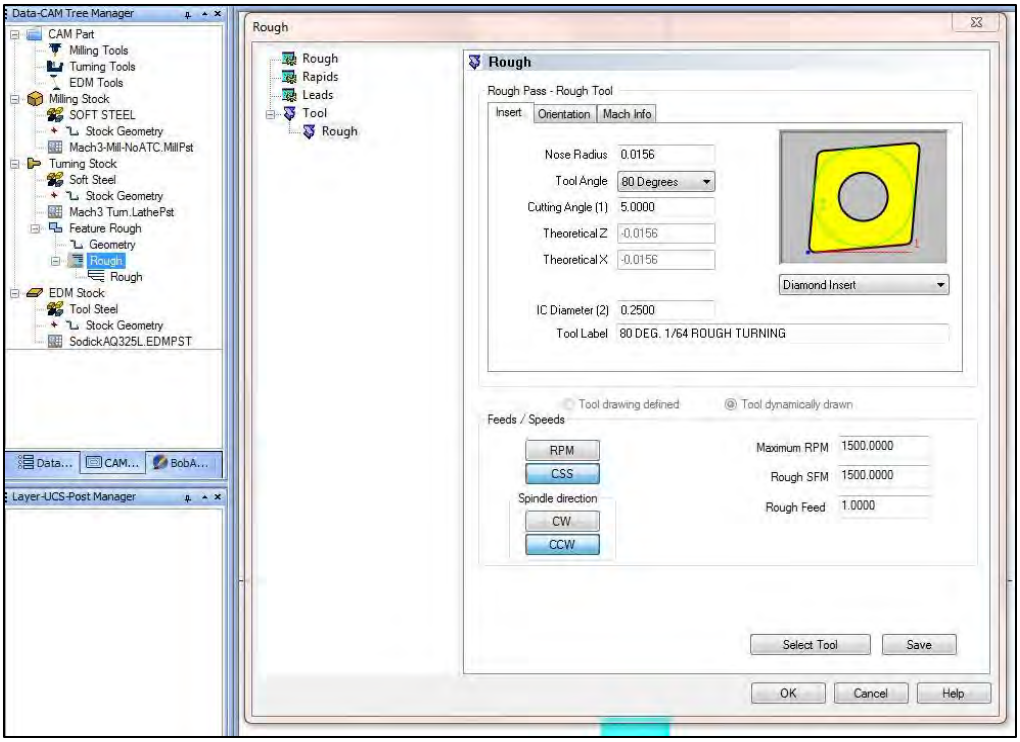

Figure 34. Setting the tool parameters.

The lathe turning speed can be set in RPM (revolutions per minute) or CSS (constant surface speed), as shown in Figure 34. Also, the feed rate and spindle speed can be entered (For Teflon, "Rough Feed" is recommended to be 0.1 inch/min). Spindle direction can be CW (clock wise) or CCW (counter clock wise) [23, 24].

"Orientation" in Figure 35 determines the side of the stock that is cut. For example "Orientation Number 1" in Figure 35 shows that stock is cut from right, and "Orientation Number 4" is used for internal diameter cutting. "Orientation Number 1" was selected for cutting the bull's-eye structure. "Mach Info" in Figure 36 shows that the tool home position ("Home position X" and "Home position Z") can be entered. The tool home position is the place where the tool goes after an operation is completed [23, 24].

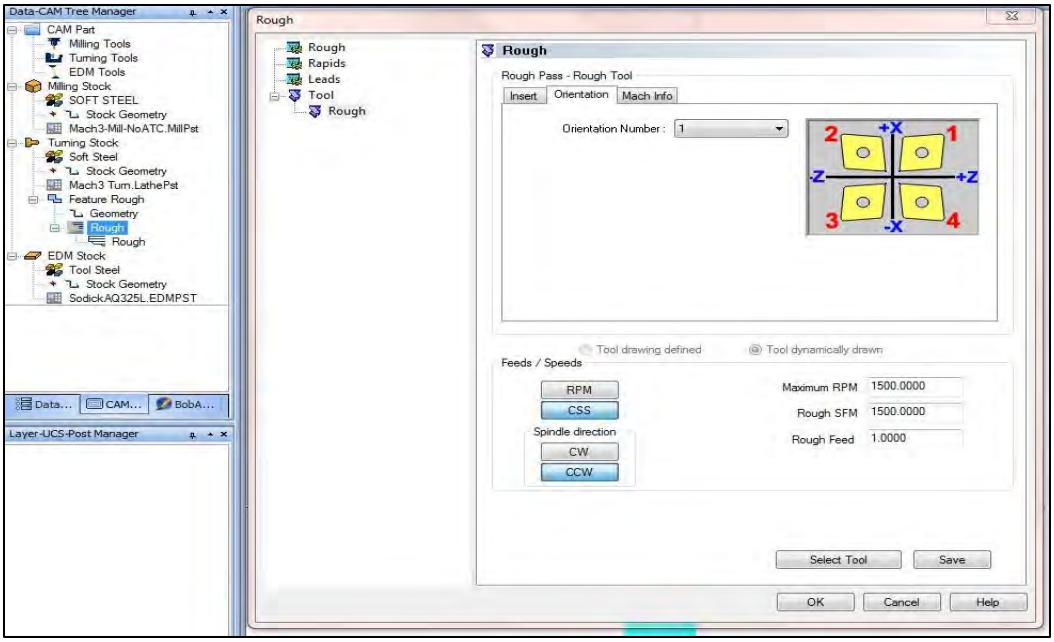

Figure 35. Setting *"*Orientation".

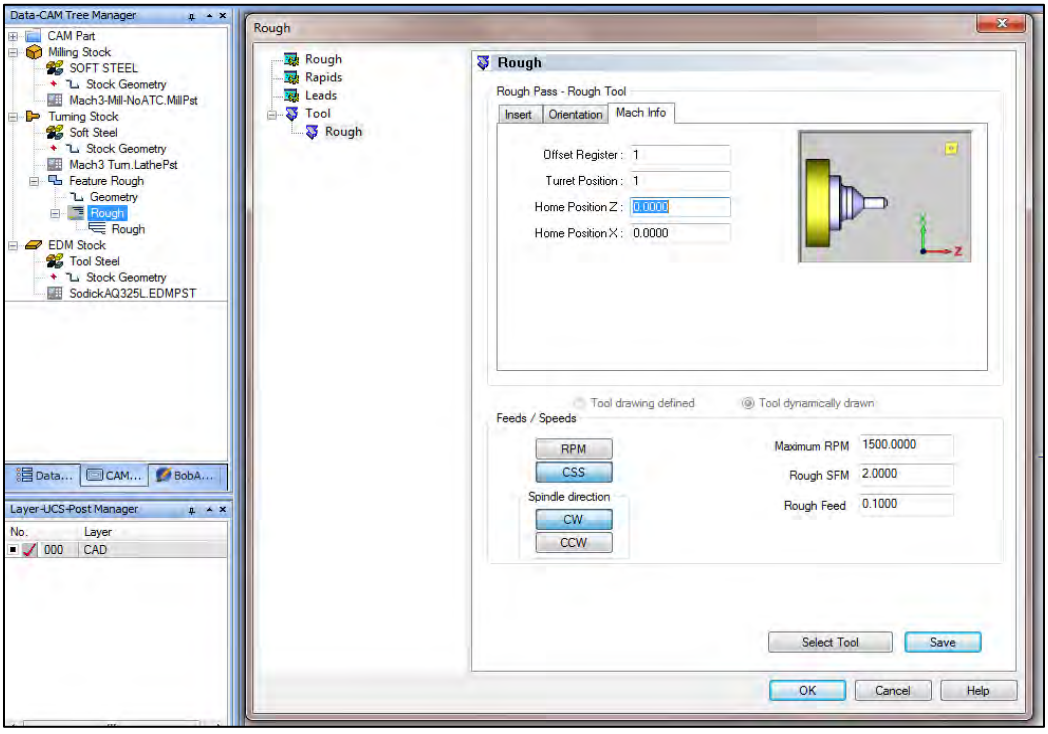

Figure 36. Setting the tool home position (Home Position Z and Home Position X).

In Figure 37, the Mach 3 post-processor was selected because a lathe CNC machine with the Mach 3 controller was used for cutting the structure. After selecting the post-processor, the G-code can be posted by right clicking on “Turning Tools”, as shown in Figure 38. The tool path on the bull’s-eye structure is shown in green in Figures 37-38 [23, 24].

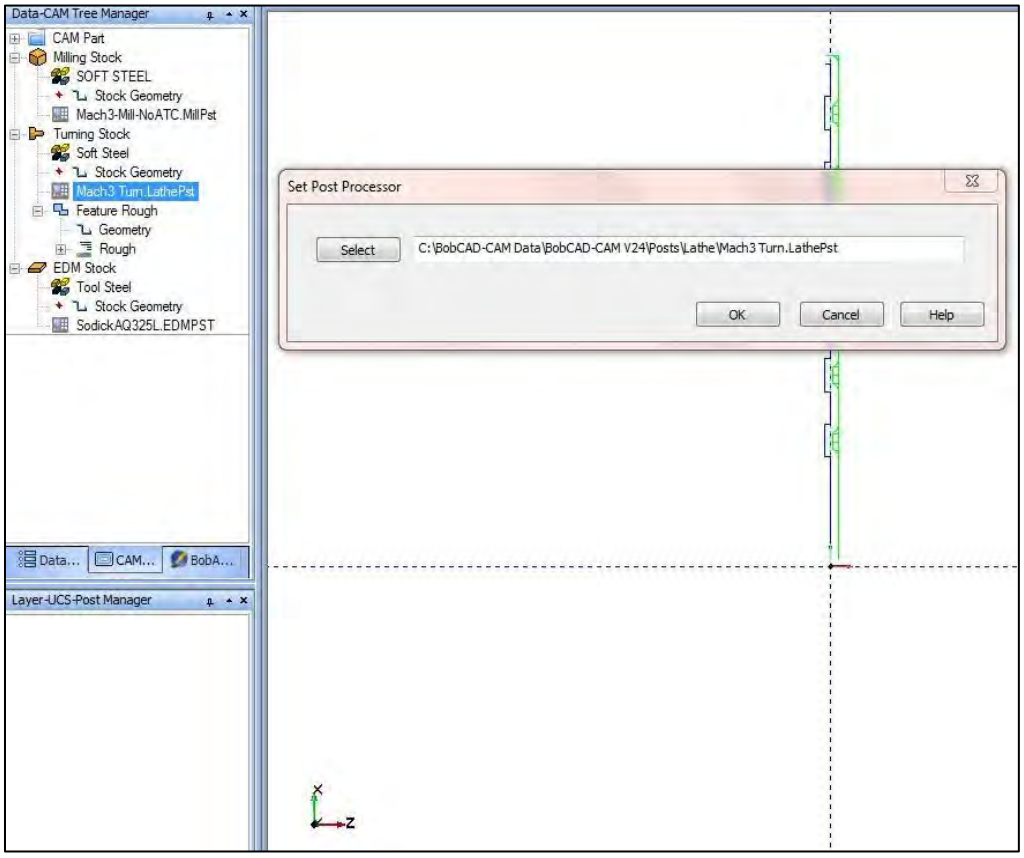

Figure 37. Selecting the post-processor.

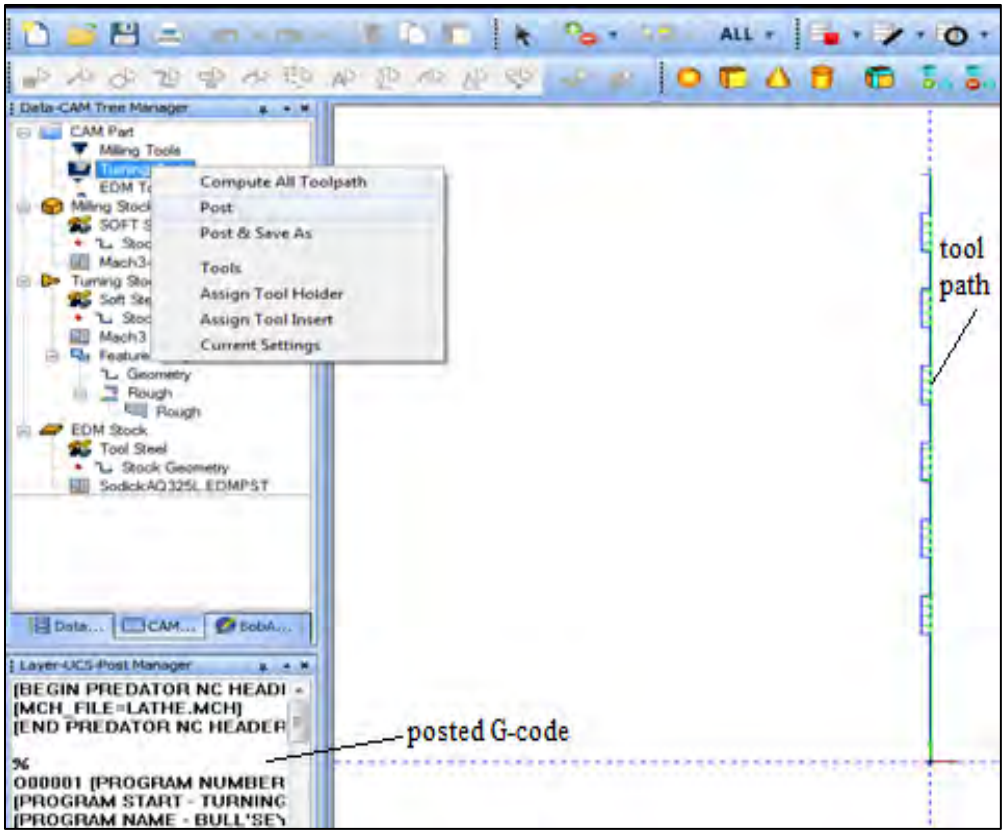

Figure 38. Posting the G-code.

Summary & Notes

One can become familiar with the general steps of programming G-code for a specific geometry by reading this appendix. However, to learn about different cutting operations in BobCAD in detail, one should refer to the professional manuals and watch the training videos available in the THz Sensors group library.

There are a number of useful points that should be mentioned regarding the two CNC machines (micro milling machine, and CNC combo-machine) in the THz Sensors group. It is not recommended to use the micro milling machine for cutting large parts because its motor and pulley belt cannot withstand much load. Also, the CNC combo-

machine controller cannot be connected to a laptop because the necessary USB cable connection can vibrate too loose when the machine is in operation, which results in a disconnection between the laptop and CNC machine controller. So a desktop computer should be used for running the CNC combo-machine. Any other observation or recommendations regarding the design, programming or operation of the machines should be added to this document and posted for future operators.

Prior to any operation of the mills or lathes, the operator must have documented safety training appropriate to the task. The operator is also responsible for the safety of any other individuals in the immediate area around the machines.

Appendix II. HFSS Meshing and Convergence

Mathematical Procedure

As explained in the third chapter, HFSS uses the FEM to solve the Maxwell equations. Figure 39 shows the procedure that HFSS follows to find the field results and S matrix for a model [17].

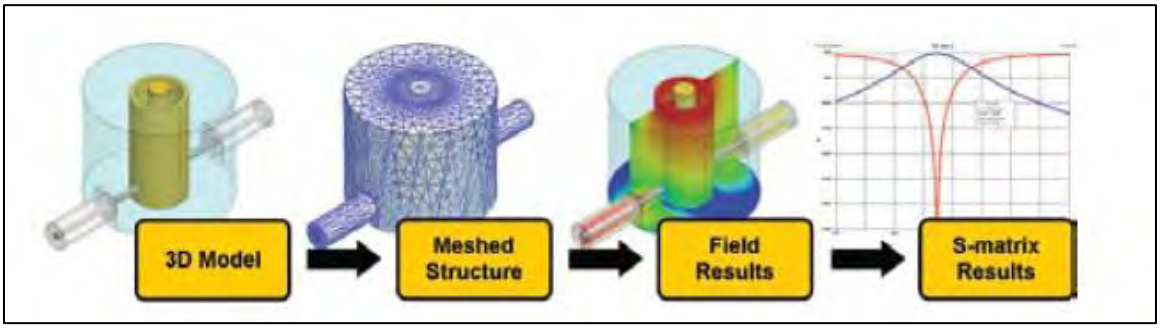

Figure 39. HFSS procedure for finding fields and S matrix [17].

HFSS uses Equation (1) [17] to find the E-field for a structure. After Equation (1) is discretized and E-field is found for each element in a meshed structure, magnetic field is found using Equation (2) [17].

$$\nabla \times \frac{1}{\mu_r} \nabla \times E - k_0^2 \varepsilon_r E = 0 \qquad (1)$$

$$H = \frac{1}{\omega \mu} \nabla \times E \qquad (2)$$

After the field values are found, S matrix is then computed. HFSS uses an adaptive solution process, which means that mesh is refined iteratively in the regions which have high E-field solution error until the solution converges to the defined convergence criterion [16, 17].

Shape Functions

HFSS uses 3D tetrahedral elements to mesh geometries. A shape function is used to interpolate the field values within an element. As shown in Figure 40, nodal field values are explicitly solved and field values within an element can be interpolated using nodal values and a shape function [16].

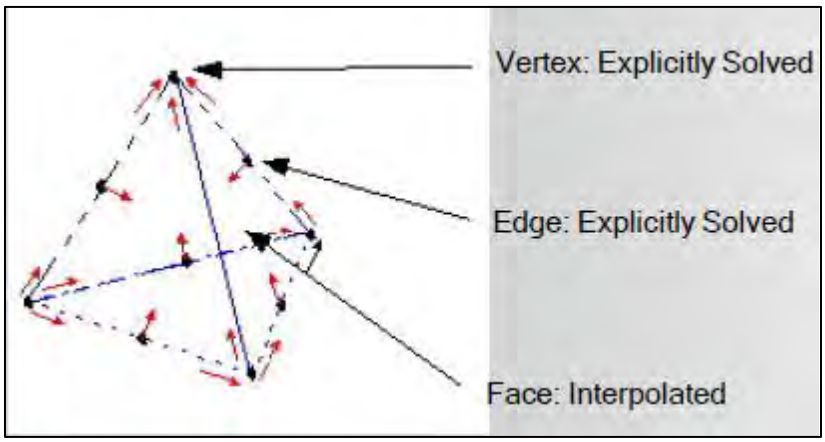

Figure 40. A 3D tetrahedral element [16].

HFSS has four different shape functions, which are zero, first, second, and mixed order shape functions. Zero order shape function is a linear function and results in a linear interpolation. First order shape function is a second order polynomial and has twenty unknowns per element. Mixed order shape function applies a mixture of shape functions

with different orders. For bull's-eye structure simulation, first order shape function was used because bull's-eye is a large structure compared to its performance wavelength, and it is recommended by the HFSS manual to use the first order shape function for such geometries [16].

Conformal Meshing

HFSS uses a conformal system of meshing. An example of a conformal mesh can be observed in Figure 41 [16].

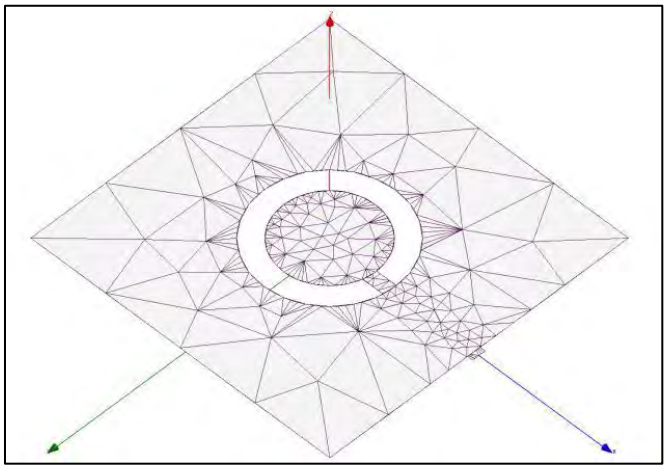

Figure 41. Conformal system of meshing [16].

As shown in Figure 41, there are a large number of elements in the specific regions of the model which have higher field variation and require higher accuracy. Fewer elements are used in the regions with lower field variation. The conformal system of meshing allows HFSS to save in simulation time by creating a large number of elements only in the regions which have high solution error while generating fewer elements in the other parts of a model [16].

Adaptive Meshing

An iterative process is used to solve fields for a designed model in HFSS. After each iterative pass, mesh is refined until ΔS converges below its user defined value. This system of refining the mesh after each iterative pass is known as the adaptive meshing. Also, an initial mesh, created for a geometry in HFSS, is dependent on the solution frequency. The mesh is refined and solved at the solution frequency. By setting a higher value for the solution frequency, a finer initial mesh will be generated for an adaptive mesh process. Using a very high solution frequency will result in increased time for simulation. For a frequency sweep analysis problem, the solution frequency can be set near the top end of the frequency range, which results in a fine mesh for the lower frequencies. For example, the solution frequency was set to 100 GHz for the 3-mm-wavelength bull's-eye structure simulation in the frequency range of 90-100 GHz [16].

Convergence Criterion

The S parameters for the current mesh of a model are compared to the previous mesh. If the change in the S parameters (ΔS) is less than the user defined value, the iterative process terminates, which shows that the current mesh is fine enough to yield an accurate solution. ΔS is used as a criterion to determine the mesh convergence and is defined in Equation (3) [18].

$$\Delta S = Max_{ij}[mag\ S_{ij}^{N} - S_{ij}^{N-1}\ ] \quad (3)$$

In Equation (3), i and j covers all S matrix entries and N shows the iterative pass number. The default value for ΔS is 0.02 (2%), but it can be as low as 0.01 (1%).

Selecting values for ΔS less than 0.01 is not necessary and only increases the simulation time. Convergence to the defined value for ΔS does not guarantee the accuracy of obtained results, and a user should also check the progress of iterative process toward the convergence. ΔS can be plotted versus iterative pass number. After each iterative pass, mesh is refined. So, ΔS should decrease as the number of passes increases. A correct convergence profile can be observed in Figure 42 [18].

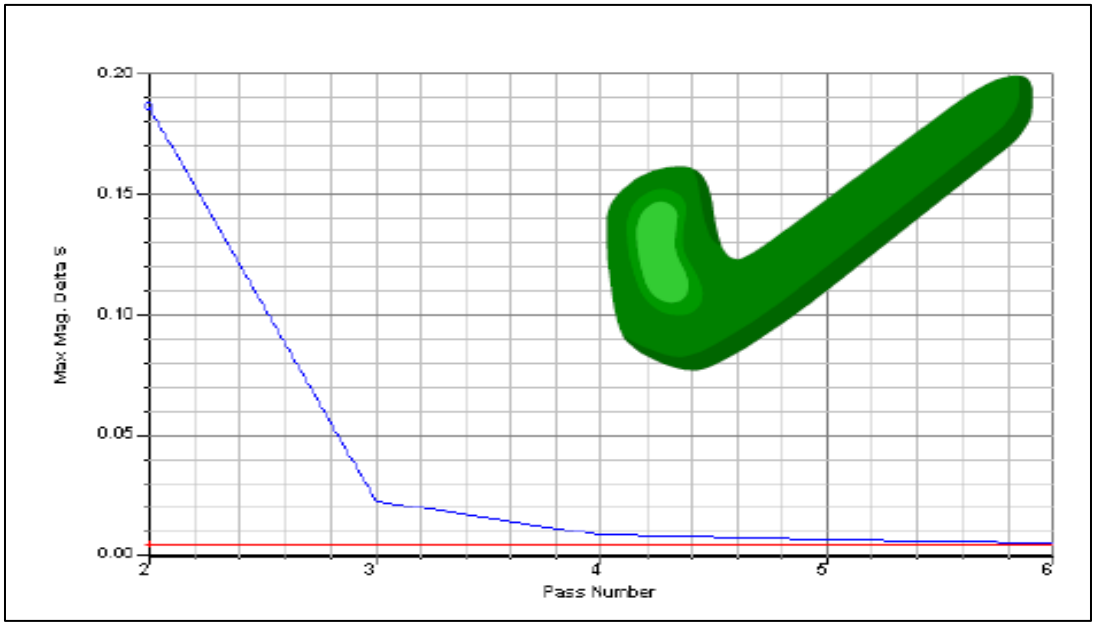

Figure 42. A correct convergence profile [18].

A correct convergence profile is a decreasing profile. A solution with a changing convergence profile is not accurate. A changing convergence profile is shown in Figure 43. A changing profile can be the result of a poor mesh quality and wrong assignments of excitations and boundary conditions to a model [18].

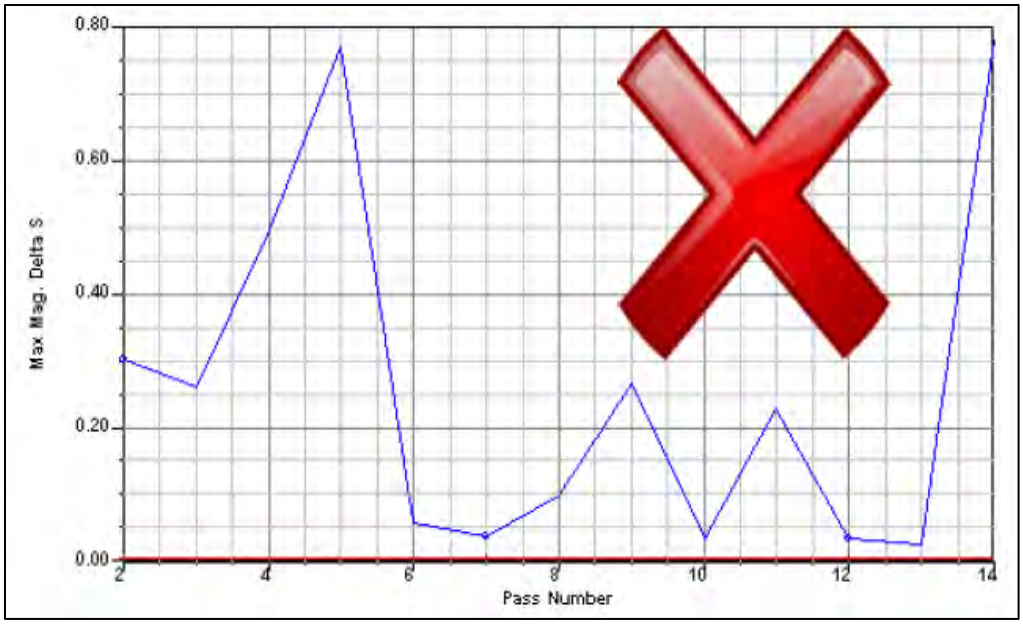

Figure 43. A changing convergence profile [18].

In the case of having a changing convergence profile for a solution, the obtained results are not right, even if the solution converges to the user defined value for ΔS [18].

REFERENCES

1. Ishihara, K., Ohashi, K., Ikari, T., Minamide, H., Yokoyama, H., Shikata, J.-, & Ito, H. (2006). Terahertz-wave near-field imaging with subwavelength resolution using surface-wave-assisted bow-tie aperture. *Applied Physics Letters*, *89*(20).
2. Jansen, C., Wietzke, S., Peters, O., Scheller, M., Vieweg, N., & Salhi, M., … Koch, M. (2010). Terahertz imaging: applications and perspectives. *Applied Optics*, *49*(19), E48-E57.
3. Bethe, H. A. (1944). Theory of diffraction by small holes. *Physical Review*, *66*(7-8), 163-182.
4. Bouwkamp, C. J. (1950). On the diffraction of electromagnetic waves by small circular disk and holes. *Philips Research Reports*, 5-321.
5. Adam, A.J.L. (2011). Review of near-field terahertz measurement methods and their applications: How to achieve sub-wavelength resolution at THz frequencies. *Journal of Infrared, Millimeter, and Terahertz Waves*, *32*(8-9), 976-1019.
6. Mitrofanov, O., Lee, M., Hsu, J. W. P., Pfeiffer, L. N., West, K. W., Wynn, J. D., & Federici, J. F. (2001). Terahertz pulse propagation through small apertures. *Applied Physics Letters*, *79*(7), 907-909.

7. Shi, X., & Hesselink, L. (2002). Mechanisms for enhancing power throughput from planar nano-apertures for near-field optical data storage. *Japanese Journal of Applied Physics*, 41, 1632-1635.

8. Tanaka, K., & Tanaka, M. (2003). Simulation of an aperture in the thick metallic screen that gives high intensity and small spot size using surface plasmon polariton. *Journal of Microscopy*, 210(3), 294-300.

9. Jin, E. X., & Xu, X. (2004). Finite-difference time-domain studies on optical transmission through planar nano-apertures in a metal film. *Japanese Journal of Applied Physics*, 43, 407-417.

10. Thio, T., Pellerin, K. M., Linke, R. A., Lezec, H. J., Ebbesen, T. W. (2001). Enhanced light transmission through a single subwavelength aperture. *Optics Letters*, *26*(24), 1972-1974.

11. Thio, T., Lezec, H. J., Ebbesen, T. W., Pellerin, K. M., Lewen, G. D., Nahata, A., & Linke, R. A. (2002). Giant optical transmission of sub-wavelength apertures: physics and applications. *13*(3).

12. Lezec, H. J., Degiron, A., Devaux, A., Linke, R. A., Martin-Moreno, L., Garcia-Vidal, F. J. & Ebbesen, T. W. (2002, AUGUST 2). Beaming light from a subwavelength aperture. *Science*, *297*, 820-822.

13. Akarca-Biyikli, S., Bulu, I., & Ozbay, E. (2004). Enhanced transmission of microwave radiation in one-dimensional metallic gratings with subwavelength aperture. *Applied Physics Letters, 85*(7), 1098-1100.

14. Mahboub, O., Carretero Palacios, S., Garcia-Vidal, F. J., Rodrigo, S. G., Martin-Moreno, L., & Ebbesen, T. W. (2010). Optimization of bull's eye structures for transmission enhancement. *Optics Express*, *18*(11), 11292-11299.

15. Ishihara, K., Ikari, T., Minamide, H., Shikata, J., Ohashi, K., Yokoyama, H., & Ito, H. (2005). Terahertz near-field imaging using enhanced transmission through a single subwavelength aperture. *Japanese Journal of Applied Physics*, *44*(29), L929-L931.

16. HFFS Advanced Course, Chapter 2 – Solution Process Review, © ANSYS Inc., 2011.

17. An Introduction to HFSS: Fundamental Principles, Concepts, and Use, © Ansoft, LLC., 2009.

18. HFFS Advanced Course, Chapter 3 – Meshing and Convergence, © ANSYS Inc., 2011.

19.

20. Töpfer, F., Dudorov, S. N., & Oberhammer, J. (2012). Micromachined 100 GHz near-field measurement probe for high-resolution microwave skin-cancer diagnosis. *IMS 2012 International Microwave Symposium*, Montreal, QC, Canada.

21. BobCAD-CAM Version 24 Training Professor & Video Series, Copyright © 2011 by BobCAD-CAM Inc.

22. Post processors. Retrieved from http://bobcad.com/support/post-processors.

23. V24 getting started: Lathe drawing example. Retrieved from http://bobcad.com/videos/bobcad-cam.

24. V24 getting started: Lathe programming. Retrieved from http://bobcad.com/videos/bobcad-cam.